

CALIBRATION OF NEBULAR EMISSION-LINE DIAGNOSTICS: II. ABUNDANCES

M. S. OEY

Space Telescope Science Institute, 3700 San Martin Drive, Baltimore, MD 21218, USA; oey@stsci.edu

J. C. SHIELDS

Ohio University, Dept. of Physics and Astronomy, Clippinger Research Labs. 251B, Athens, OH 45701-2979, USA; shields@helios.phy.ohiou.edu

Submitted to ApJ 17 January 2000; accepted 17 March 2000

ABSTRACT

We examine standard methods of measuring nebular chemical abundances, including estimates based on direct T_e measurements, and also emission-line diagnostics. We use observations of the LMC H II regions DEM L199, DEM L243, DEM L301, and DEM L323, whose ionizing stars have classifications ranging from O7 to WN3. Following common practice, we assume a two-zone T_e structure given by $T(O^{++})$ and $T(O^+)$ to compute ionic abundances. We compare with photoionization models tailored to the observed properties of the individual objects, and emphasize the importance of correctly relating T_e in the two zones, which can otherwise cause errors of ~ 0.2 dex in abundance estimates. The data show no spatial variations or local metallicity enhancements to within 0.1 – 0.15 dex in any of the objects, notably including DEM L199, which hosts three WR stars.

Our data agree well with both the modeled $R23$ and $S23$ abundance diagnostics for O and S. We present the first theoretical tracks for $S23$, which are in excellent agreement with a larger available dataset. However, contrary to earlier suggestions, $S23$ is much *more* sensitive to the ionization parameter (U) than is $R23$. This occurs because $S23$ does not sample S IV, which is often a significant population. We therefore introduce $S234 \equiv ([S\ II] + [S\ III] + [S\ IV])/H\beta$, and demonstrate that it is virtually independent of U . Predicted and observed spatial variations in $S234$ are thus dramatically decreased in contrast to $S23$. The intensity of $[S\ IV]\lambda 10.5\mu$ can be easily estimated from the simple correspondence between $[S\ IV]/[S\ III]$ and $[O\ III]/[O\ II]$. Using this method to estimate $S234$ for data in the literature yields excellent agreement with our model tracks, hence we give a theoretical calibration for $S234$. Our models show that the double-valued structure of $S23$ and $S234$ remains an important problem as for $R23$, and presently *we consider calibrations of these S diagnostics reliable only at $Z \lesssim 0.5 Z_\odot$* . However, the slightly larger dynamic range and excellent compatibility with theoretical predictions suggest the S parameters to be more effective abundance diagnostics than $R23$.

Subject headings: galaxies: abundances — galaxies: ISM — H II regions — ISM: abundances — Magellanic Clouds — supernova remnants

1. INTRODUCTION

The emission-line signatures of H II regions are a powerful and widely-used indicator of galactic abundances. This is especially true in distant galaxies where most stellar abundance probes cannot be employed. Furthermore, the spectral properties of H II regions also give important diagnostics of the ionizing stellar population, such as effective temperature and numbers of stars. Given the wide use of such nebular diagnostics, it is vital to test and calibrate them using H II regions with known characteristics and ionizing stellar populations.

Along with a companion paper (Oey et al. 2000; hereafter Paper I), we report here on a detailed study for this purpose, of four H II regions in the Large Magellanic Cloud (LMC). The OB associations in all four of these H II regions have been examined in detail and classified, thereby strongly constraining the ionizing energy distributions. In addition, the LMC's proximity and orientation with respect to the Galaxy also permit a detailed understanding of the nebular morphology. Thirdly, the abundances can be accurately determined. We therefore have high-quality information on the three principal parameters that determine the nebular emission: stellar effective temperature

(T_*), the ionization parameter (U) that relates ionizing flux to gas density, and metallicity (Z).

Table 1 gives a brief summary of our objects, which can be examined in greater detail in Paper I. The first two columns in Table 1 give the H II region identification in the Davies, Elliott, & Meaburn (1976) and Henize (1956) H α catalogs, respectively; the third column identifies the parent OB association from Lucke & Hodge (1970). Column four shows the spectral type of the dominant ionizing stars, as classified by the references in column 8. Column five lists the nebular H α luminosity from Oey & Kennicutt (1997), and column 6 shows the adopted value from Paper I, of the inner radius of the gas distribution, as a fraction of the Strömgren radius R_S . This gives some indication of the nebular morphology. Finally, column 7 indicates the presence of significant shock excitation: DEM L243 includes an embedded or superimposed supernova remnant (SNR), and DEM L301 also shows evidence of significant shock activity (Paper I). While shocks may be present in the other objects as well, their contribution to the nebular emission is unimportant.

The detailed presentation of the objects is given in Paper I, including narrow-band images in H α , [O III], and [S II], and spectroscopic observations over the wavelength

range 3500 – 9200 Å. For each object, we observed two to three stationary, spatially-resolved slit positions. For all of the objects except DEM L301, we also obtained spatially integrated observations by scanning the long slit across the nebulae. The scanned data should therefore resemble typical observations of such H II regions at distances of 10 – 20 Mpc. As seen in Table 1, the sample spans a range in dominant stellar spectral types, from O7 to early Wolf-Rayet (WR). There is also variety in the morphology of the objects, ranging from near perfect Strömgren sphere (DEM L323), to extreme shell structure (DEM L301), to highly complex (DEM L199).

Paper I provides a detailed analysis of the spatially resolved emission-line ratios with respect to the sequence in T_\star represented by these objects, and a comparison with photoionization models using the current generation of stellar atmosphere models for both O stars and early WR stars. In general we found a gratifyingly high level of agreement, largely supporting the CoStar energy distributions of Schaerer & de Koter (1997) and early WR atmospheres of Schmutz, Leitherer, & Gruenwald (1992) and Hamann & Koesterke (1998). In conjunction with data from Kennicutt et al. (2000), we provide a first, empirical calibration of nebular diagnostics for the dominant T_\star . In addition to the well-known η' radiation softness parameter of Vílchez & Pagel (1988), we introduce [Ne III] λ 3869/H β as a similar diagnostic, which is more robust to nebular conditions and is sensitive for a higher range of T_\star .

We also presented in Paper I the spatially-resolved behavior of the O abundance parameter (Pagel et al. 1979),

$$R23 \equiv \frac{[\text{O II}]\lambda 3727 + [\text{O III}]\lambda\lambda 4959, 5007}{\text{H}\beta} \quad ; \quad (1)$$

and S abundance parameter (Vílchez & Esteban 1996; Christensen et al. 1997; Díaz et al. 1999),

$$S23 \equiv \frac{[\text{S II}]\lambda 6724 + [\text{S III}]\lambda\lambda 9069, 9532}{\text{H}\beta} \quad , \quad (2)$$

where we designate the [S II] lines λ 6716 + λ 6732 as λ 6724, analogous to [O II] λ 3727. We confirmed that both observationally and theoretically, $R23$ remains spatially uniform across the nebulae. In contrast, for uniform abundances, models of $S23$ vary across the nebulae, showing lower values in central regions. The observations clearly reflect this pattern, which is caused by the missing ionization stage of S IV. We address this issue in detail below in this paper. As is well-known, $R23$ and $S23$ are also sensitive to T_\star , and these effects are also shown in Paper I for our objects.

In this paper, we present the abundance determinations for our sample, for both the spatially-resolved and scanned longslit observations. We examine conventional assumptions for the nebular electron temperature (T_e) structure and resulting ionic and total abundance determinations. We then explore the metallicity diagnostics $R23$ and $S23$ in more detail, and introduce another diagnostic, $S234$. As before, we use the photoionization code MAPPINGS II (Sutherland & Dopita 1993) in conjunction with CoStar stellar atmosphere models (Schaerer & de Koter 1997) for O stars.

2. DIRECT ABUNDANCE DETERMINATIONS

We derived abundances from the measured line fluxes in Paper I using standard techniques. For calculation of line emissivities for elements heavier than helium, we used the five-level atom code FIVE_L as implemented in STSDAS version 1.3.5 (Shaw & Dufour 1995). We initially obtained an estimate of electron density from the [S II] λ 6716/ λ 6731 line intensity ratio, assuming a default $T_e = 10^4$ K. The densities are almost all $\lesssim 100 \text{ cm}^{-3}$.

2.1. Temperature structure

The assumed T_e structure, and thereby, ionization structure of the H II region, can generate substantial uncertainties in even “direct” abundance determinations from typical optical emission-line spectra. The T_e structure is in turn a function of density structure and stellar atmosphere models. Peimbert’s (1967) t^2 formulation for temperature fluctuations is probably the best-known example of addressing this problem, which can be used for both small-scale and large-scale variations in T_e .

We consider here the large-scale temperature structure. As discussed below, our photoionization models tend to overestimate T_e , suggesting that small-scale fluctuations are not significant. Standard abundance determinations adopt either a single characteristic T_e or a two-zone model for T_e , and these assumptions can also cause substantial errors in abundance determinations. Garnett (1992) provides one of the more thorough investigations of this issue, which is a well-known problem for elements like S that do not conform well to a two-zone model. However, if the adopted zone temperatures do not adequately characterize the respective regions, then the inferred abundance can be significantly in error even for elements like O that are well-described by a two-zone model. This can be a problem especially in cooler nebulae with $T_e \lesssim 10,000$ K, that have strong temperature gradients (Garnett 1992; Stasińska 1980).

We assumed here a two-zone temperature structure for our nebulae, such that a common T_e was adopted for excitation of O III, Ne III, S III, and Ar III; while a separate T_e was adopted for the excitation of N II, O II, and S II. We used the same electron density for both zones.

For the high ionization zone, we adopted $T(O^{++})$, the volume-averaged T_e for the O^{++} population. This is obtained essentially directly from the observed $T[\text{O III}]$, the temperature inferred from the [O III] λ 4363/(λ 4959 + λ 5007) line intensity ratio. A temperature can also be obtained in principle from the [S III] λ 6312/(λ 9069 + λ 9532) ratio. However, the auroral line flux in this case was often described by a large fractional uncertainty, which introduced correspondingly large random errors in the resulting abundances; there is also some possibility that the near-IR lines may be affected by telluric absorption (e.g., Stevenson 1994). We consequently chose to adopt $T(O^{++}) = T[\text{O III}]$ for the high-ionization zone, including the S^{++} region. Garnett (1992) has suggested on the basis of nebular models that the relation between ion-weighted temperatures for S^{++} and O^{++} is linear, but with a slope differing from unity. For objects in the current study, $T[\text{O III}]$ values are generally close to 10,000 K, at which point Garnett’s work suggests that the ion-weighted $T(S^{++})$ and $T(O^{++})$ should be similar; thermal effects of

dust in the nebula may also be expected to reduce the contrast between the two temperatures (Shields & Kennicutt 1995), lending support to use of a common value.

For the low-ionization zone, T_e can be obtained directly from the $[\text{S II}](\lambda 4069 + \lambda 4076)/(\lambda 6716 + \lambda 6731)$ ratio, but we found that this option frequently suffered from a low signal-to-noise ratio. It is often standard practice to derive the lower-ionization $T(\text{O}^+)$ from the higher-ionization $T(\text{O}^{++})$ using an analytic relation (e.g., Campbell, Terlevich, & Melnick 1986; Pagel et al. 1992), whose accuracy clearly affects that of the abundance determination. We investigated several alternatives before adopting a prescription for $T(\text{O}^+)$. In deciding what relation to adopt, our principal criterion was that the abundances input to MAPPINGS photoionization models for the individual objects (Paper I) should be consistent with those inferred from the output emission-line spectra. For example, when using the expression employed by Pagel et al. (1992, their equation 6), our resultant H II region model spectra implied an O abundance that was ~ 0.2 dex lower than the assumed input, a substantial departure from self-consistency!

The relationship between $T(\text{O}^{++})$ and $T(\text{O}^+)$ is model-dependent, and varies with ionization parameter and metallicity. Figure 1 shows $T(\text{O}^+)$ vs. $T(\text{O}^{++})$ for MAPPINGS photoionization models at $Z = 0.3 Z_\odot$, with an inner radius of $0.4 R_S$. The different symbols correspond to different CoStar stellar atmospheres as indicated, with B2, C2, and E2 corresponding to spectral types O8–O9, O6–O7, and O3–O4, respectively. We show models with $\log U = -2, -3, \text{ and } -4$. The dashed and dot-dashed lines show the relation between $T(\text{O}^+)$ and $T(\text{O}^{++})$ from Campbell et al. (1986; see also Garnett 1992), and Pagel et al. (1992), respectively, while the dotted line delineates $T(\text{O}^+) = T(\text{O}^{++})$.

The Pagel et al. relation deviates significantly from the models at these temperatures, while the Campbell et al. relation shows reasonable agreement in slope for $T(\text{O}^{++}) > 10,000$ K, falling close to the theoretical predictions for $\log U = -3$. At lower temperatures, the models are more consistent with an isothermal nebula. We consequently adopted the formulation,

$$T(\text{O}^+) = \begin{cases} 0.7 T(\text{O}^{++}) + 3000 \text{ K} , & T(\text{O}^{++}) > 10,000 \text{ K} \\ T(\text{O}^{++}) , & T(\text{O}^{++}) < 10,000 \text{ K} \end{cases} \quad (3)$$

where $T(\text{O}^{++}) = T[\text{O III}]$ as described above. The relation for $T(\text{O}^{++}) > 10,000$ K is that given by Campbell et al. Equation 3 yields consistent input and output abundances to $\lesssim 0.05$ dex, except for Ne, whose modeled line ratios are persistently discrepant with the observations (Paper I; see below). We caution that Figure 1 and equation 3 are optimized in the parameter space relevant to our LMC targets. Different formulations may be more appropriate at other metallicities and ionization parameters; it is beyond the scope of this work to fully examine this issue. However, it is clear that some care is necessary in choosing a relation between $T(\text{O}^{++})$ and $T(\text{O}^+)$.

While we ensured consistency between the input and output abundances to the photoionization models, one worrisome problem that remains unresolved is the over-prediction of T_e in comparison to the observations, as presented in Paper I. To briefly summarize, the predicted

$T[\text{O III}]$ is greater than that inferred from the observed $[\text{O III}]\lambda 4363/\lambda 5007$ by 850 K in DEM L323 and 1500 K in DEM L199. The problem may also exist in the other two objects, DEM L243 and DEM L301, but the fainter emission from $\lambda 4363$ in these lower-excitation nebulae prevented any useful constraints. We also found that the discrepancy persisted when using Hummer & Mihalas (1970) stellar atmosphere models and the CLOUDY (Ferland 1998) photoionization code. Since $T(\text{O}^{++})$ and $T[\text{O III}]$ agree to $< 1\%$ in the models, the effect is not caused by non-collisional excitation of $\lambda 4363$ in the models. As discussed in Paper I, the temperature discrepancy occurs in lines of sight across the entire nebulae, and is in the *opposite* sense of that expected from small-scale temperature fluctuations (Peimbert 1967). Our sample therefore shows *no* evidence that such T_e fluctuations systematically bias our abundance determinations. Mathis (1995) discusses evidence for and against the general existence of significant T_e fluctuations.

2.2. Ionic abundances

Determining ionic abundances relative to H requires calculation of the $\text{H}\beta$ emissivity, which is also temperature dependent, but originates in both the high- and low-ionization zones. We adopted an intermediate temperature for calculation of the $\text{H}\beta$ emissivity, representing an average of $T(\text{O}^{++})$ and $T(\text{O}^+)$, weighted by the relative abundances of O^{++} and O^+ . The same intermediate temperature was used for computing He emissivities, using expressions taken from Benjamin et al. (1999). This construction was used to obtain ionic abundances from the line measurements in Paper I, which were corrected for reddening and, where necessary, underlying Balmer absorption. The abundance results for different nebular lines of a single ion were combined, weighted by the variance of the line fluxes.

Total abundances were obtained from the ionic abundances following the standard practice of using ionization correction factors (ICFs) to allow for unobserved ionization stages. We employ the following relations:

$$\frac{\text{O}}{\text{H}} = \frac{\text{O}^+ + \text{O}^{++}}{\text{H}^+} \quad , \quad (4)$$

where the lack of detectable He II $\lambda 4686$ emission indicates no significant O^{+3} population;

$$\frac{\text{N}}{\text{H}} = \frac{\text{N}^+}{\text{O}^+} \cdot \frac{\text{O}}{\text{H}} \quad (5)$$

(Peimbert & Costero 1969; Garnett 1990); and

$$\frac{\text{S}}{\text{H}} = \left[\frac{\text{S}^+ + \text{S}^{++}}{\text{H}^+} \right] / \text{ICF}(\text{S}^{+3}) \quad , \quad (6)$$

where

$$\text{ICF}(\text{S}^{+3}) = \left[1 - \left(1 - \frac{\text{O}^+}{\text{O}} \right)^\alpha \right]^{1/\alpha} \quad , \quad (7)$$

with $\alpha = 2.5$, corrects for unobserved S^{+3} ions (Garnett 1989; Stasińska 1978). For the noble gases, we adopt

$$\frac{\text{Ne}}{\text{H}} = \frac{\text{Ne}^{++}}{\text{O}^{++}} \cdot \frac{\text{O}}{\text{H}} \quad (8)$$

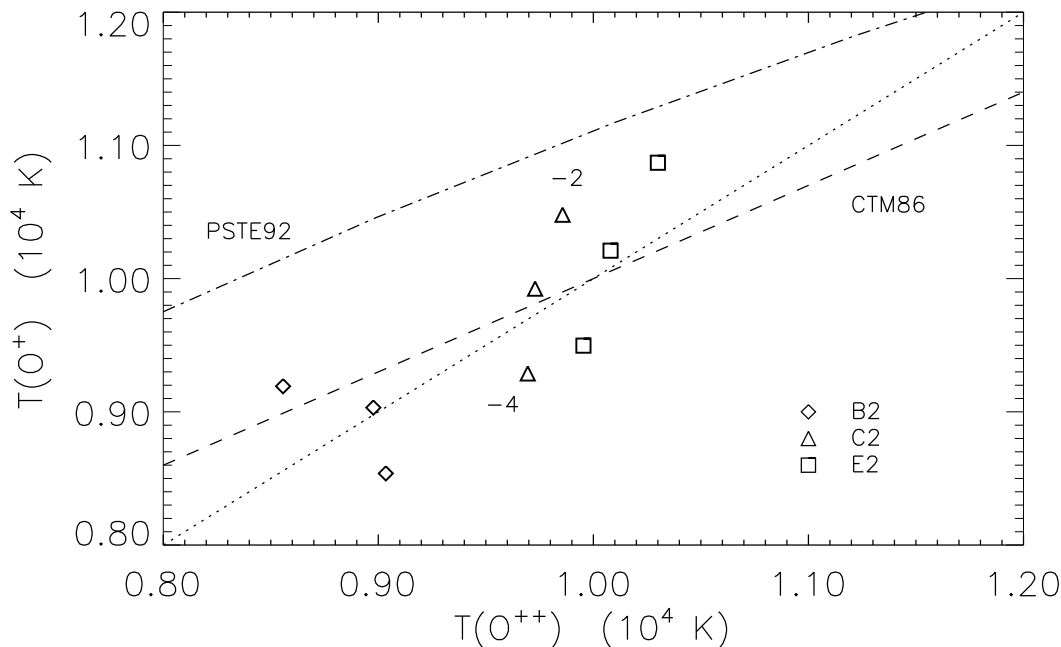


FIG. 1.— $T(\text{O}^+)$ vs. $T(\text{O}^{++})$ from photoionization models. The symbols correspond to models using the indicated CoStar stellar atmospheres (see text). The locus of results for $\log U = -2, -3,$ and -4 fall in the sense indicated for the C2 runs. We overplot dashed and dot-dashed lines that show the relations of Campbell et al. (1986) and Pagel et al. (1992), respectively; the dotted line shows $T(\text{O}^+) = T(\text{O}^{++})$.

(Peimbert & Costero 1969; Simpson et al. 1995), and

$$\frac{\text{Ar}}{\text{H}} = \frac{\text{Ar}^{++}}{\text{S}^+ + \text{S}^{++}} \cdot \frac{\text{S}}{\text{H}} \quad (9)$$

(Garnett et al. 1997). Most of our objects are ionized by early-type stars (Table 1), thereby fully ionizing He, but not exhibiting detectable He II. Thus our default relation for He is simply,

$$\frac{\text{He}}{\text{H}} = \frac{\text{He}^+}{\text{H}^+} \quad (10)$$

For DEM L243, which is ionized by O7 stars, the He I $\lambda 5876/\text{H}\beta$ line ratios suggest that He is not fully ionized throughout the nebula (Paper I; see below). For this object, we experimented with the expression for He/H given by Peimbert & Torres-Peimbert (1977; their equation 15), that includes an ICF for He^0 ; however, this prescription yields He abundances that are at least 0.1 dex higher than the rest of the objects in the sample. We therefore give results for DEM L243 using equation 10 and note that these should be treated as lower limits to the true abundance. It is worth remarking that our investigation supports the results of Baldwin et al. (1991), who find that the Orion He abundance was slightly overestimated by Peimbert & Torres-Peimbert as a result of their ICF for He^0 .

The theoretical support for use of equations 4–9 derives mostly from models that consider the integrated properties of H II regions (e.g., Garnett 1992; Mathis 1985; Stasińska 1978). Thus, observations that sample only a small “pencil-beam” through a nebula may not yield the correct abundances if such an analysis scheme is used; Gruenewald & Viegas (1992) have discussed this problem in de-

tail. However, previous observational studies have found generally good agreement in elemental abundances derived at variable positions across individual nebulae, using the integrated-spectrum methods (e.g., Díaz et al. 1987; Masegosa, Moles, & del Olmo 1991; González-Delgado et al. 1994). Such agreement was found even when substantial excitation gradients were seen within the H II region. In the present study, we can directly compare abundances obtained from the integrated spectrum of a nebula with those calculated by the same means from small-aperture measurements at a variety of radii. We show below in §2.3.1 that we find a high degree of consistency between the different aperture measurements for the same source, including the integrated spectrum. These results support the validity of using integrated-spectrum prescriptions when only a part of the H II region is observed. Apparently the characteristic physical parameters determined for the two ionization zones are adequate to determine the ionic abundances to high accuracy in our objects.

2.3. Abundance results

We used the prescriptions above to compute abundances for both the spatially resolved and scanned, spatially integrated observations for each object. Table 2 presents results for the individual, spatially resolved observations, along with error estimates. These were obtained from the uncertainties in measured fluxes, using a Monte Carlo method similar to that described by Kobulnicky & Skillman (1996). Input flux values were modified randomly by addition of Gaussian noise with amplitude corresponding to $1-\sigma$ measurement uncertainties, for a total of 5000

iterations per spectrum. A few points with low signal-to-noise ratios yielded unphysical solutions in the T_e and abundance determinations, and these were discarded from the sample. The standard deviation of the resulting abundance distribution was adopted as the final uncertainty.

Table 3 presents the mean values of the spatially-resolved measurements, weighted inversely by the variances. We also list the corresponding formal uncertainty in the mean. Note that the weighting scheme and quoted errors assume that actual variations are negligible in the quantities listed in Table 3, and that the scatter results from a normal distribution of measurement errors. As described below, we do not find significant evidence for abundance fluctuations; however, it is possible that the measurement errors may not be a strictly normal distribution. The listed errors in Table 3 are therefore likely to somewhat underestimate the true uncertainties, nor do these include systematic errors.

Regarding the abundances of Ne, it is important to note that there is probably a substantial systematic error in the values obtained in Table 3, and also later in Table 4. As discussed in Paper I, the observed line intensities for Ne are systematically discrepant with the tailored models. Although earlier generation stellar atmospheres caused [Ne III] intensities to be underpredicted, we now find a modest overprediction. The discrepancy can be resolved by reducing $\log(\text{Ne}/\text{H})$ by 0.2 – 0.3 dex. However, since we do not understand the cause of the discrepancy, we have chosen to list the Ne abundance derived from the standard relations. It appears likely that errors in the stellar atmospheres are responsible for much of the problem (Paper I). Peimbert (1993) also emphasizes the uncertainty in equation 8. The high ionization potential (40.96 eV) required for Ne III gives it outstanding potential for probing hot stellar ionizing sources, so it is highly desirable to resolve the uncertainties regarding its emission.

2.3.1. Spatial uniformity

In Figure 2*a–e*, we show the spatial distribution of elemental abundances across the sightlines for our stationary observations of DEM L199. Figure 2*f* shows the corresponding distribution in $T[\text{O III}]$ measurements. For DEM L243, DEM L301, and DEM L323, we show in Figures 3–5 the results for He, N, and O, as representative of the other elements. These are shown respectively in panels *a*, *b*, and *c*; and panels *d* show corresponding measurements of $T[\text{O III}]$. The different symbols correspond to individual slit positions as designated in Paper I (Figures 6, 8, 12, and 13), to aid cross-referencing. Following our convention in that work, we simply show the slit positions superposed, therefore these figures will not necessarily show clean radial profiles across the nebulae, although they do approximate this reasonably well. This issue may be inspected in Paper I, along with actual slit positions. The light, horizontal lines indicate the spatial extent of each extracted aperture, while the vertical error bars indicate uncertainties in the derived measurements.

In Figure 3, DEM L243 shows much larger scatter and uncertainty among the individual apertures, which can be attributed to the large measurement uncertainties for $T[\text{O III}]$ (Figure 3*d*). There is also an SNR either embedded or superimposed in the line of sight to this object, but we have not included the affected apertures in

our abundance estimates or in Figure 3. Assuming an essentially constant metallicity in DEM L243, we recomputed the abundances by fixing $T(\text{O}^{++})$ to be the mean $T[\text{O III}]$, using the same weighting and omitting the same deviant values as before, in computing the mean abundances. Figure 6 and Table 3 show the results using the new $T(\text{O}^{++})=9700$ K. The dramatic reduction in scatter for the heavy elements suggests that the original scatter in Figure 3 may indeed be caused by poor measurements in $T[\text{O III}]$. However, we emphasize a point by Mathis, Chu, & Peterson (1985), that true abundance fluctuations will induce corresponding fluctuations in T_e , owing to the more efficient cooling accompanying higher O/H. The reduced scatter with a fixed T_e is therefore not a strong demonstration of truly constant abundances. To further test consistency with constant abundance distributions, we computed the reduced- χ^2 statistics for the original distribution, yielding 1.4 and 1.8 for $\log(\text{N}/\text{H})$ and $\log(\text{O}/\text{H})$, respectively. The probabilities of obtaining these values for 12 degrees of freedom are 16% and 4%, respectively. These values therefore hint that the scatter may in part be caused by real variations, although the significance is low.

In the event that the abundances for DEM L243 are essentially constant, the mean values obtained with fixed $T[\text{O III}]$ should give a better estimate than the original values (Table 3). However, we caution that there is systematic uncertainty introduced by the adopted value of $T(\text{O}^{++})$; comparison to the original mean abundances in Table 3 suggests the uncertainty is roughly 0.1 dex in the derived metallicities. Since the recombination lines used to determine $\log(\text{He}/\text{H})$ are less temperature-sensitive than the collisional metal lines, $\log(\text{He}/\text{H})$ (Figure 6*a*) still shows larger scatter than exhibited in the other objects. However, note that the magnitude of the variation is only ~ 0.3 dex. As discussed in Paper I, the He I $\lambda 5876/\text{H}\beta$ ratios suggest that He is not uniformly fully ionized in DEM L243, therefore causing $\log(\text{He}/\text{H})$ to be underestimated in many apertures. Our value for the He abundance is therefore a lower limit in this object. The upper envelope to the distribution in Figure 6*a* is around $\log(\text{He}/\text{H}) \sim -1.1$, which may be more indicative of the true He abundance. This value is more consistent with those for the other objects (Table 3).

Thus, in Figures 2–5 the abundances appear to show no spatial variations within the measurement uncertainties, with standard deviations typically around 0.10 – 0.15 dex. The uniformity of the abundance derivations is reassuring, and suggests that our adopted ionic relations (§2.2) and description of the nebular temperature structure (equation 3) yield abundance estimates with high accuracy. The apparent success of these methods is consistent with the finding by Mathis (1985) that ICFs for model nebulae appear fairly robust between volume averaged and radially averaged regions. The uniformity of results for apertures tracing different parts of the same nebula further suggests that spurious “pencil-beam” effects resulting from projection of radial T_e gradients (Gruenwald & Viegas 1992) are negligible for our objects. This is consistent with the fact that sources in our sample have $T[\text{O III}]$ restricted to the approximate range 9500 – 12,000 K, for which the nebulae are expected to be relatively isothermal (equation 3; Figure 1). We emphasize that this propitious cir-

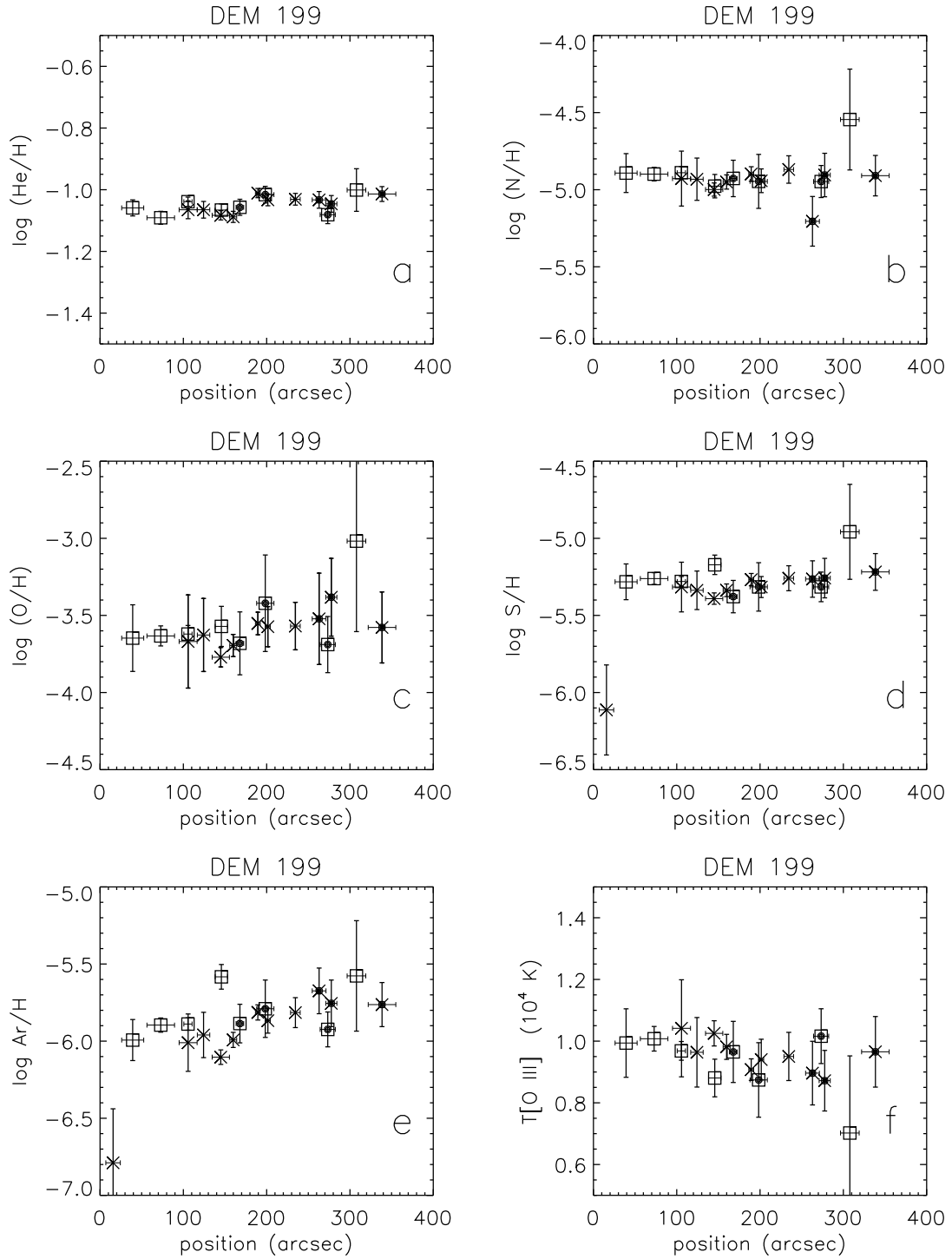


FIG. 2.— Spatial variation in abundances and $T[\text{O III}]$ along the slit positions for DEM L199. Light, horizontal lines show aperture sizes, while vertical error bars indicate abundance uncertainties. An LMC distance of 50 kpc corresponds to $0.24 \text{ pc arcsec}^{-1}$. Apertures near WR stars are highlighted with solid dots.

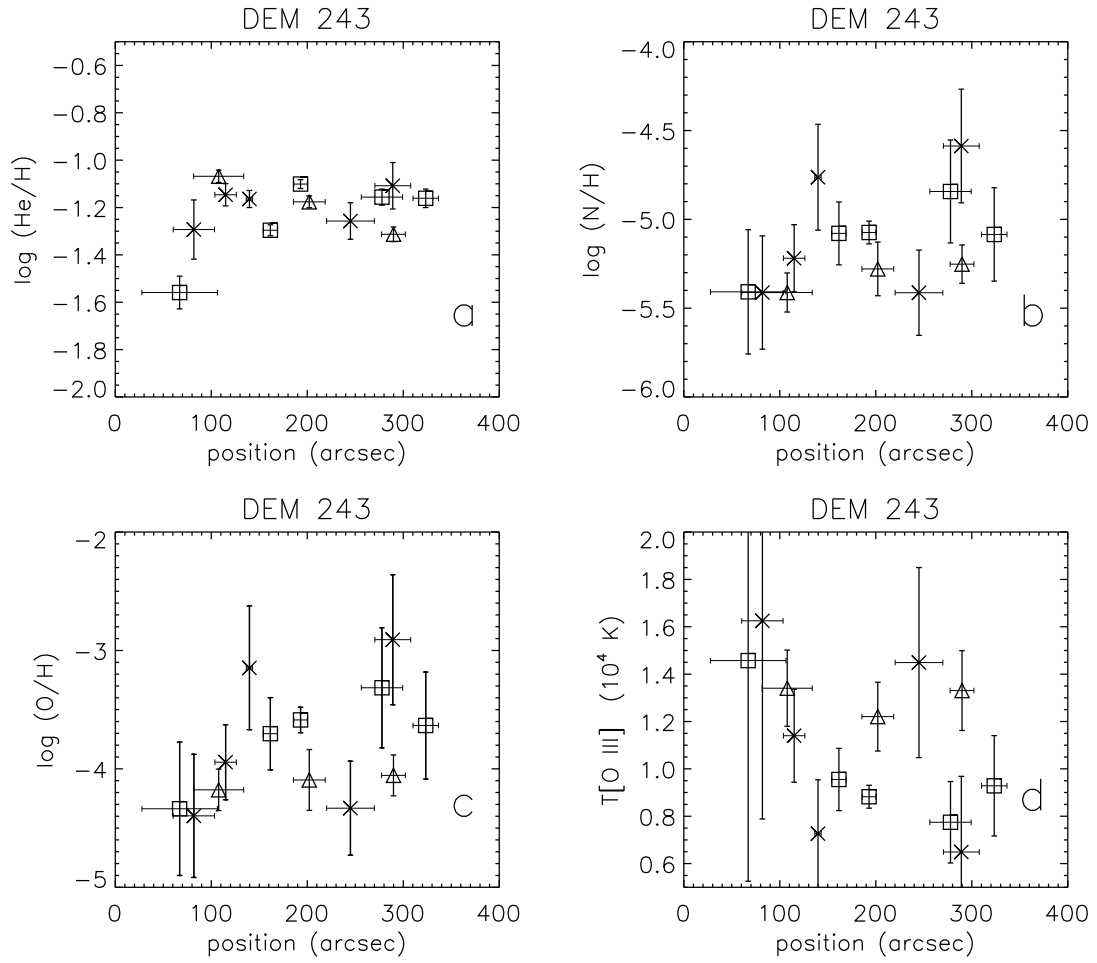


FIG. 3.— Spatial distribution for $\log(\text{He}/\text{H})$, $\log(\text{N}/\text{H})$, $\log(\text{O}/\text{H})$, and $T[\text{O III}]$ for DEM L243. The notation is as in Figure 2, but note the different scales. Apertures affected by the SNR are omitted. Values of $\log(\text{He}/\text{H})$ should be considered lower limits for this object.

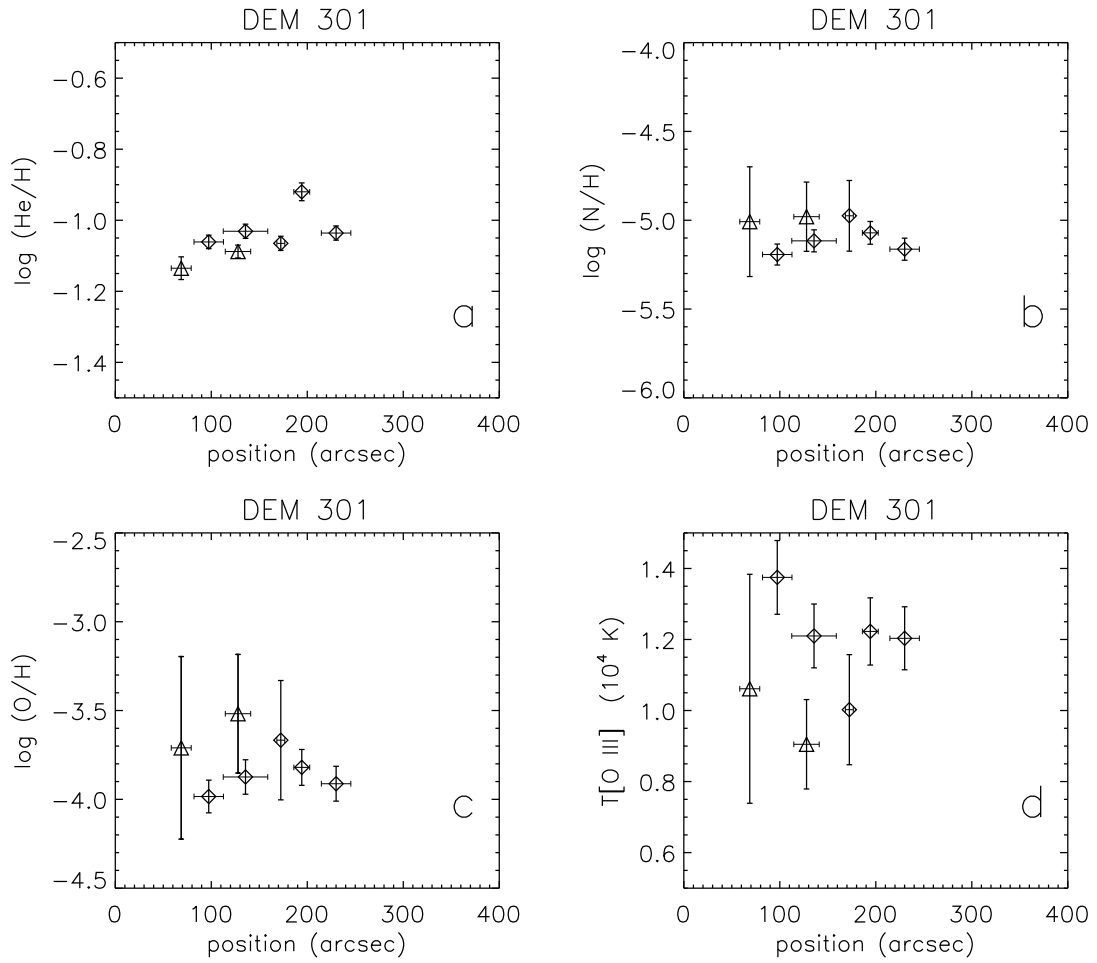


FIG. 4.— Same as Figure 3, for DEM L301. Note the ordinate scales are as in Figure 2.

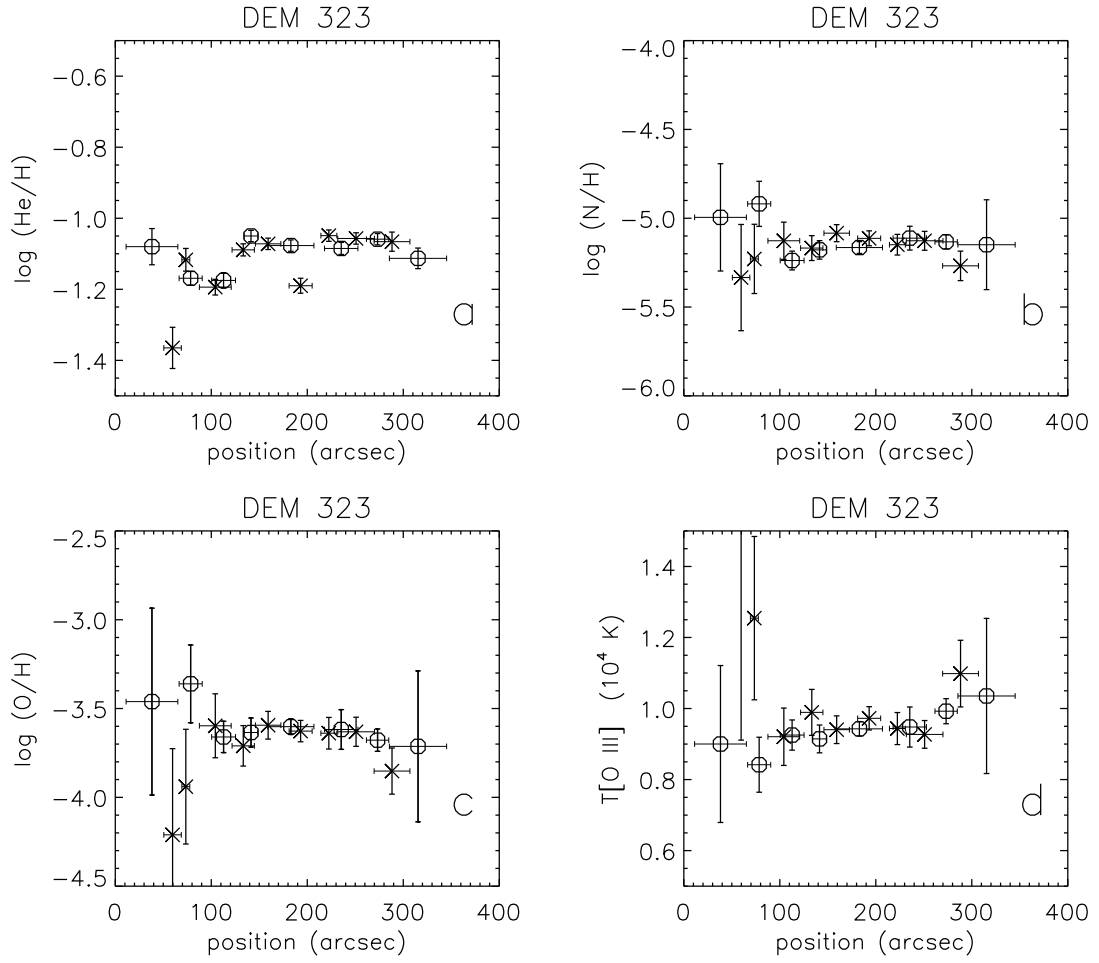


FIG. 5.— Same as the previous Figure, for DEM L323.

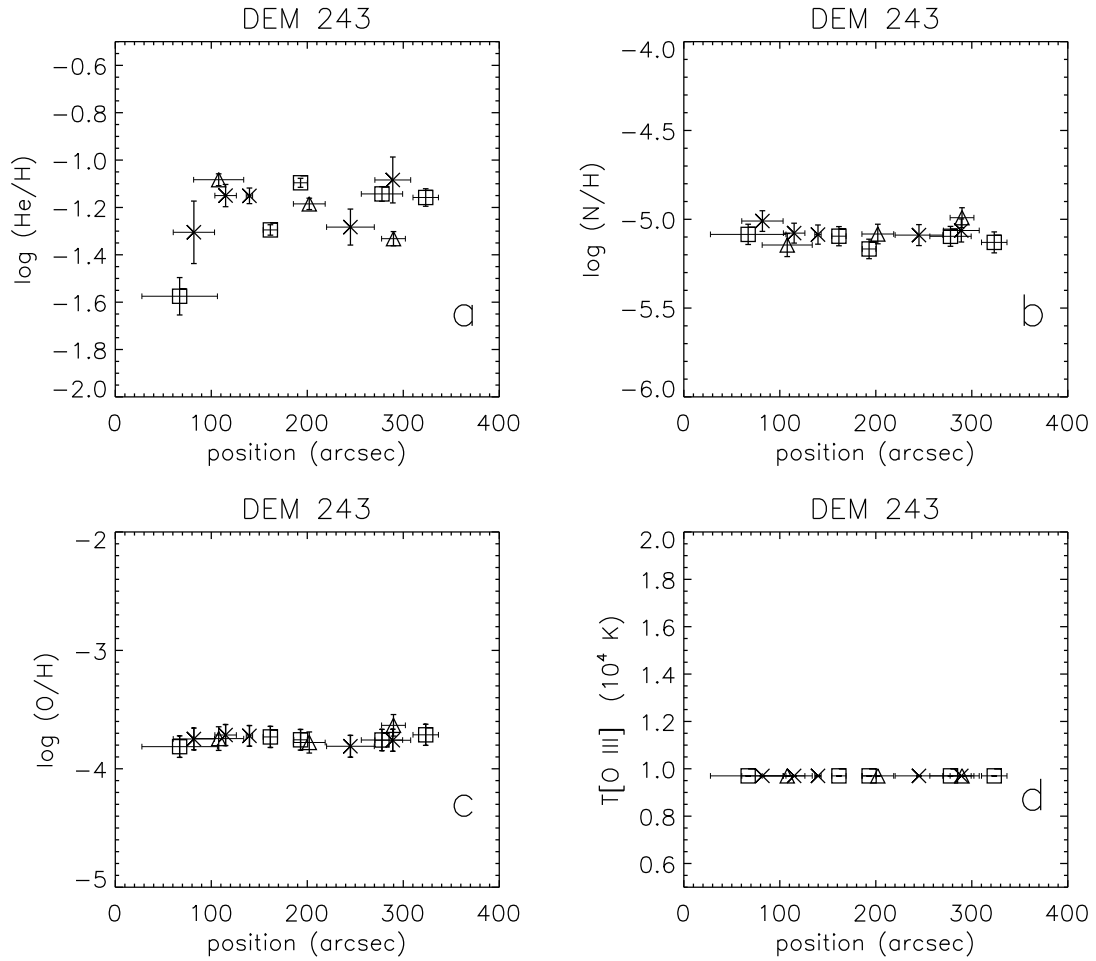


FIG. 6.— Data for DEM L243 as in Figure 3, but with $T(\text{O}^{++})$ fixed at 9700 K for all included apertures.

cumstance may not apply to other H II regions, that may exhibit stronger T_e gradients; as an example, Walter, Dufour, & Hester (1992) reported a significant T_e gradient in the Orion nebula, although their spatial scale of 0.5 pc is almost an order of magnitude smaller than is relevant for our objects in the present study. As in §2.1 above, we again emphasize the importance of choosing the correct parameterization for the T_e structure.

2.3.2. Search for self-enrichment

It is especially interesting to examine DEM L199 for possible abundance variations that are introduced by the three WR stars. Two of these are binaries with a WN3 component (Breysacher 1981) and one is a WC4 + O6 V-III binary (Moffat et al. 1990). The exact location of these stars with respect to the nebular gas distribution and slit positions may be examined in Paper I. We emphasize that DEM L199 is not a WR ejecta shell, but is a large, luminous H II complex whose dominant ionizing stars are early WR stars. Walsh & Roy (1989) and Kobulnicky et al. (1997) identified two regions in the starburst galaxy NGC 5253 that appear to show enhanced N, which is suggested to result from self-enrichment by WR stars. Kobulnicky et al. (1997) point out that accompanying He enrichment would be expected from the WR sources, and acknowledge that the lack of He excess in these objects is puzzling.

DEM L199 has three WR stars within a large central cavity in a luminous H II region. It would seem likely that, if self-enrichment from WR stars can be seen, it should be detected in our observations. In Figure 2, we indicate six apertures that are closest to the stars Br 32 (WC4) and Br 33 (WN3), with solid dots. These apertures are identified in Paper I as: D199.205-15, 16, and 17; and D199.205N120-17, 18, and 19. The characteristic physical distances from the WR stars are about 5 – 15 pc. Figure 2 shows that these points do not show any sign of abundance enhancements. Results from the full set of aperture measurements for DEM L199 are consistent with uniform abundances at the 90% confidence level, as indicated by reduced- χ^2 values of 0.59 and 0.60, for $\log(N/H)$ and $\log(O/H)$ respectively, with 17 degrees of freedom. For He, in particular, the variation is constrained to be $\lesssim 0.1$ dex. Although abundance enhancements are seen in WR ejecta nebulae, our data suggest that self-enrichment by WR stars can be an extremely subtle phenomenon. It is possible that the processed material is heated to coronal temperatures within the superbubble and is thus optically undetectable. Alternatively, the WR phase in these stars may not yet have lasted long enough to produce significant enrichment in the surrounding environment.

We were also interested to see whether the SNR in DEM L243 showed evidence of abundance anomalies. Abundance estimates from SNRs are necessarily more uncertain, owing to the more complicated radiative transfer, but meaningful estimates have been made by, e.g., Russell & Dopita (1990). These are based on matching the emission-line spectra with a shock code. In Paper I, we were able to find excellent agreement between MAPPINGS shock models and the observed emission from the shock-affected apertures, using the abundances derived from the uncontaminated regions of the nebula listed in Table 3. The SNR therefore shows no evidence of abundance anomalies, al-

though strong emission from photoionized gas in the same line of sight prevents strong constraints.

Likewise, the superbubble DEM L301 shows strong evidence of a recent SNR impact (Chu & Mac Low 1990; Oey 1996b; Paper I), and thus could conceivably show enrichment by massive star winds and supernova ejecta. However, its elemental abundances are often lower than for the other objects in the sample (Table 3). We caution that shock-excitation can significantly affect the abundance determinations for this object (Paper I). Peimbert, Sarmiento, & Fierro (1991) showed that contamination by shock activity can cause abundances to be underestimated, especially for higher-ionization species. Our measurements for DEM L301 are consistent with this behavior, although in §2.3.3 we find that the metallicities for DEM L243 do not appear strongly affected by SNR contamination.

2.3.3. Spatially integrated abundances and LMC metallicities

We also derived abundances for the scanned, spatially integrated apertures using the same methods. These are presented in Table 4, along with mean LMC H II region abundances from compilations by Dufour (1984). A more recent compilation by Garnett (1999) shows essentially the same values. Within the uncertainties, the mean abundances for each object from Table 3 agree with the determinations from the spatially integrated observations (Table 4), although the offsets appear to be systematic across all elements for each object. This again points to uncertainties in the $T(O^{++})$ determination, which can result from simple measurement errors, or factors related to the spatial integration of the line emission. We regard the values obtained from the mean of the spatially resolved data (Table 3) to be more reliable than the single observations from the integrated data. However, we caution that the ionic relations in §2.2 are based on spatially integrated models and observations, and this could introduce systematic variations between the spatially resolved and scanned data. But taking the derived values and uncertainties at face value, the mean abundances of the stationary apertures should be somewhat more reliable.

We include in Table 4 the abundances for DEM L243 derived from both the total, scanned observation and the scanned observation with the SNR-contaminated region subtracted. Interestingly, there is no significant difference between these, although the data including the SNR do show the expected decrease in computed abundances (Peimbert et al. 1991). Thus, while DEM L301 showed suspiciously low metallicity measurements attributable to effects of shock emission, DEM L243 is an example where the SNR is not a significant factor. In Paper I, we also found that the two shock-affected objects exhibit different behavior in their line emission with respect to the photoionized regions, thereby demonstrating how shocks contribute in different ways to the spectra of host H II regions, depending on shock velocity and environment.

We find a tendency for our measurements to be ~ 0.2 dex lower than the mean LMC metal abundances compiled by Dufour (1984). One of the probable causes is our adopted temperature structure (equation 3), which varies slightly from those used by others. For example, we find that our mean abundances for DEM L243 would increase

by about 0.1 dex if we adopted the relation of Campbell et al. (1986) at all values of $T(\text{O}^{++})$.

Our data are generally consistent with there being no abundance variations between the four different H II regions. It is interesting to note that DEM L199 is close to the LMC bar, about 1 kpc from the center of the galaxy; and DEM L243 is situated in the northern outskirts of the LMC-4 supergiant shell, at a galactocentric radius of ~ 3.5 kpc. Pagel et al. (1978) have suggested that the LMC H II regions possibly exhibit a slight abundance gradient. This has not been further examined, nor has a gradient been detected in the cluster population (Olszewski et al. 1991). In our data, it is suggestive that DEM L199 and DEM L243 delineate the extremes of any interpreted variation among our four objects. The difference in metallicity is consistent with the small gradient suggested by Pagel et al. (1978).

3. SEMI-EMPIRICAL BRIGHT-LINE METHODS

We turn now to examining more indirect emission-line diagnostics of metal abundances. In situations where T_e cannot be adequately constrained by observation, it is common practice to estimate the metal abundances using the semi-empirical, “bright-line” abundance parameters. Here we examine the performance of these parameters in light of our detailed nebular data and highly-constrained, tailored photoionization models from Paper I.

We also compute model tracks of the abundance parameters, using MAPPINGS II with generalized nebular parameters. These incorporate the stellar energy distribution of CoStar model C2 (Schaerer & de Koter 1997), which corresponds to an O6 – O7 stellar effective temperature. We assume an inner radius to the gas distribution of $0.4R_S$, and gas density $n = 10 \text{ cm}^{-3}$. In the figures that follow, the dashed, solid, and dotted lines correspond to the volume-averaged $\log U = -2, -3, \text{ and } -4$, respectively, which is equivalent to changing the total ionizing photon emission rate or gas filling factor.

The grid of models is computed with $Z = 0.05, 0.1, 0.3, 0.5, 1.0, \text{ and } 2.0$ times Z_\odot . We included the elements (He, C, N, O, Ne, Mg, Al, Si, S, Ar, Ca, and Fe) with $Z_\odot = (-1.01, -3.44, -3.95, -3.07, -3.91, -4.42, -5.53, -4.45, -4.79, -5.44, -5.88, \text{ and } -4.96)$, respectively. We largely follow McGaugh (1991) in scaling the abundances of individual elements with respect to O. For He and N, we use the relations given by McGaugh, but scaled to match the Anders & Grevesse (1989) values for Z_\odot :

$$\text{He}/\text{H} = 0.0850 + 15(\text{O}/\text{H}) \quad (11)$$

and

$$\log(\text{N}/\text{H}) = 1.5 \log(\text{O}/\text{H}) + 0.66 \quad (12)$$

For C and Fe, we adopt McGaugh’s relations directly (his equations 10 and 11). The remainder of the elements are fixed in their proportion to O at Z_\odot , as given by Anders & Grevesse. Models for Z_\odot and $2Z_\odot$ use the CoStar C2 atmosphere at solar metallicity, while the rest use the corresponding SMC metallicity model; we find that the stellar metallicity is unimportant for these U -tracks.

3.1. $R23$

The O abundance parameter $R23$ (Pagel et al. 1979; equation 1 above), has been extensively used and empiri-

cally calibrated several times, by McGaugh (1991), Skillman (1989), and Dopita & Evans (1986), among others. In Figure 7a, we show $\log(\text{O}/\text{H})$ vs. $\log R23$, with the tracks showing results from generalized photoionization models described above. Our assumptions differ somewhat from those of previous studies, in particular with the assumption of a fairly hollow morphology and new stellar atmosphere models. Most authors (e.g., McGaugh 1991; Dopita & Evans 1986) also assume some anticorrelation between the characteristic T_* or U , and Z , in their adopted calibration at high abundance. Our tracks do not assume this anticorrelation. Despite these differences, our tracks remain similar to those of previous authors, although our models show a slight offset to higher $\log(\text{O}/\text{H})$ (see Kobulnicky et al. 1999 and McGaugh 1991 for comparisons of $R23$ calibrations).

We also plot in Figure 7a the spatially integrated data for our objects, using the abundances derived from the means of our resolved apertures (Table 3). The values of $R23$ are computed in Paper I and shown here in Table 5. We caution that the nebular fractional area included in the spatial scans varies among the four objects, and we refer the reader to Paper I for the precise details. The three spatial scans of the spherical object DEM L323 (triangles) should give an indication of the degree to which subsampling is representative of the total spatial scan (solid triangle). The three measurements of $R23$ are in excellent agreement, which is consistent with our finding in Paper I that this index is robust to spatial variations. For DEM L243, we show $R23$ derived from the spectrum with the SNR-contaminated region subtracted (solid diamond); and also that from the total integrated region including the SNR (open diamond). The square and cross show DEM L199 and DEM L301, respectively.

Our data points are generally well-behaved with respect to the model tracks in Figure 7a. While we found excellent agreement between the observed emission-line spectra and our tailored photoionization models in Paper I, we see in Figure 7a that most of the objects fall in their expected location with respect to the more generalized model tracks. DEM L323, DEM L243, and DEM L199 fall between tracks of $\log U = -3$ and -4 , with DEM L199 showing the highest value of U , as expected in this high-excitation object. The one anomalous point is DEM L301 (cross), which we found in Paper I to have an unusual combination of excitation mechanisms. We concluded that this object, which has an extreme shell morphology, is most likely ionized by a combination of density-bounded photoionization plus shocks. While our tailored model for this object reproduced the observed $R23$ well, it is apparent that its value is anomalously high with respect to the tracks in Figure 7a. Ironically, the offset is in the sense of a higher ionization parameter, although the object in fact has a much lower U than the others in the sample. The larger value of $R23$ is probably caused by the enhanced emission contributed by the shock activity. DEM L301 and DEM L199 have similar values of $R23$, which, lacking any additional information for these objects, would imply similar abundances; we see that in fact this would overestimate $\log(\text{O}/\text{H})$ for DEM L301 by about 0.3 dex, taking the measured $\log(\text{O}/\text{H})$ at face value.

We also overplot with small plus signs in Figure 7a the data compiled by Díaz & Pérez-Montero (2000). These

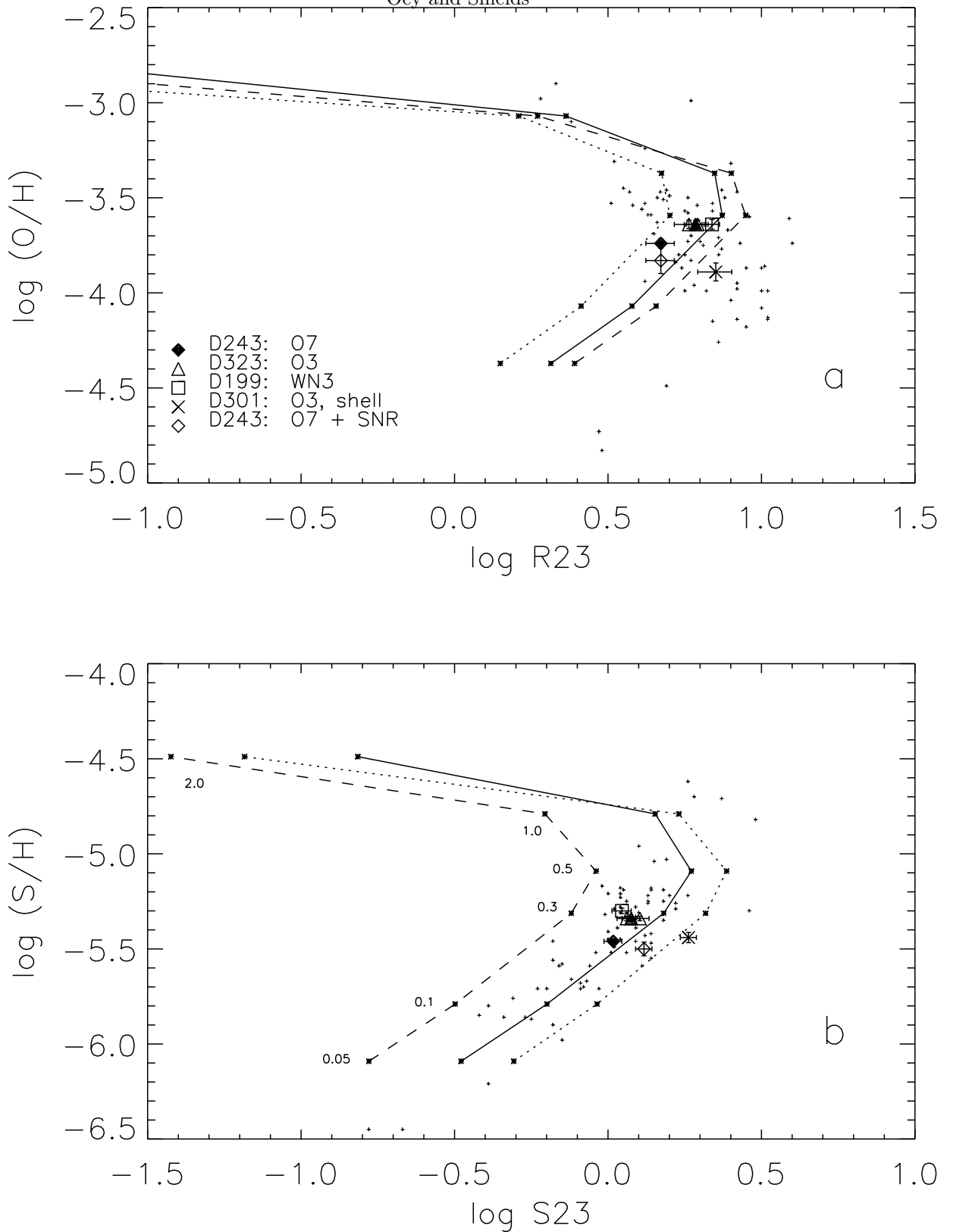


FIG. 7.— Abundance parameters $\log R23$ (panel *a*) and $\log S23$ (panel *b*) vs. $\log(O/H)$ and $\log(S/H)$, respectively. The tracks indicate photoionization models for 0.05, 0.1, 0.3, 0.5, 1.0, and $2.0Z_{\odot}$, as labeled in panel *b*. The dashed, solid, and dotted linetypes correspond to $\log U = -2$, -3 , and -4 , respectively. Our observations are indicated by the symbols shown in the key; the solid triangle corresponds to observations for DEM L323 scanned over the entire object, while the open triangles represent partial scans (see Paper I). The small plus signs show data compiled by DPM, for objects whose abundances are determined using direct measurements of T_e .

represent data from the literature (their Table 2) for which abundances were derived from a direct measurement of $T[\text{O III}]$. Although the points for our data from Paper I are consistent with the model tracks, it is apparent that the photoionization models in Figure 7a do not track well the locus of the larger dataset. It is important to note that adopting softer stellar atmospheres can improve the correspondence slightly, since this would offset the tracks to slightly lower $\log(\text{O}/\text{H})$. We refer the reader to McGaugh (1991) to evaluate the consequences of the stellar effective temperature. The atmospheres adopted here (CoStar C2) correspond to O6 – O7 stars, which are already cooler than most of our LMC objects, and only relatively small changes result if O3 – O4 atmospheres (CoStar E2) are used instead. The discrepancy between models and data has always been a difficulty in the use of $R23$, and therefore empirical calibrations of this parameter have been crucial for its successful use.

3.2. $S23$

As mentioned earlier, a parameter similar to $R23$ has been introduced for S by Vílchez & Esteban (1996) and Christensen et al. (1997), which was further explored by Díaz & Pérez-Montero (2000, hereafter DPM). It is important to note that this parameter, $S23$ (equation 2), is *not* strictly analogous to $R23$. While O and S have homologous energy levels, the ionization potentials (IP) for their respective ions are different. In particular, it is important to note that the IP required to reach S^{+3} (34.83 eV) is virtually identical to that necessary for O^{++} (35.12 eV). Therefore, although S^+ and S^{++} are indeed the dominant ions for S, for typical H II regions, there is likely to be non-negligible S^{+3} , which is ionized by the same radiation that produces O^{++} . Although Christensen et al. (1997) pointed out that the ionization fraction of S^{+3} is relatively small, typically $\lesssim 0.2$, we show below that it nevertheless significantly affects the ionization balance of S^+ and S^{++} , and consequently, the value of $S23$.

Figure 7b is similar to panel a, now showing $\log(\text{S}/\text{H})$ vs $\log S23$ (Table 5). The model line types and data symbols are the same as before. It is immediately apparent that, contrary to earlier claims in the literature, $S23$ is *more* sensitive to the ionization parameter than $R23$. The change in $\log S23$ between the model tracks, varying $\log U$ from -2 to -4 , is almost 0.5 dex, whereas it is less than 0.3 dex for $R23$. The greater U -sensitivity of $S23$ is caused by the “missing” contribution of S IV. Figure 7b shows that the models with high U show lower $\log S23$, the opposite pattern to $R23$. This is consistent with the ionization behavior of S, since a larger population of S^{+3} is expected at higher U .

As suggested by DPM, the lower-metallicity branch of $S23$ does span a larger range in values than $R23$, for a given range of Z (Figure 7). However, the location of the inflection at the maximum $S23$ is at only a slightly higher Z than that for $R23$. Figure 7 shows that our models for $\log R23$ have a maximum close to $Z = 0.3 Z_{\odot}$, and those for $\log S23$ have a maximum around $Z = 0.5 Z_{\odot}$. Thus, there is only ~ 0.2 dex extension in the dynamic range of Z in the use of $S23$. Nevertheless, since so many of the observed objects in the literature have abundances around $0.3 - 0.5 Z_{\odot}$, this augmentation makes a substantial difference in evaluating abundances. As is dramatically shown

in Figure 1 of DPM, $S23$ empirically shows an evidently monotonic increase as a function of Z , in contrast to $R23$, which shows a distinct double-valued structure in Z .

Our data points are again reasonably consistent with the models in Figure 7, although they now perhaps show a tendency to fall between the $\log U = -2$ and -3 models, rather than -3 to -4 for Figure 7a. The tailored photoionization models and spatially-resolved data in Paper I showed similar minor discrepancies. The data points for the shock-affected regions, DEM L301 (cross) and the SNR-contaminated observation for DEM L243 (open diamond) are offset to higher $\log S23$. This suggests that $S23$ is increased by the presence of shock excitation, similar to the behavior of $R23$ found in the previous section.

We also see in Figure 7b that the photoionization models do track the data well for $S23$, and much better than for $R23$ in panel a. However, it is also apparent that the points with the highest values of $S23$ fall outside the model tracks. In formulating a calibration for $S23$, we would therefore recommend that these values be excluded, and that the empirical calibration derived by DPM should not be used for $Z \gtrsim 0.5 Z_{\odot}$.

3.3. $S234$

As discussed in the previous section, the population of S^{+3} , which is ionized by the same radiation as that ionizing O^{++} , is not sampled by the $S23$ parameter. While the ionization fraction of S^{+3} is relatively small, we have seen in the previous section that it significantly compromises the utility of $S23$ as an abundance diagnostic. We therefore suggest that the parameter,

$$S234 \equiv \frac{[\text{S II}]\lambda 6724 + [\text{S III}]\lambda\lambda 9069, 9532 + [\text{S IV}]\lambda 10.5\mu}{\text{H}\beta} \quad (13)$$

is a better abundance indicator than $S23$. In the same way that $R23$ samples all significant ions of O, $S234$ more completely samples the significant ions of S. Note that any population of S^{+4} (IP 47.30 eV) will be an insignificant fraction of the total S ions, for massive star sources: $\text{S}^{+4}/\text{S} \lesssim 0.02$ even for an object ionized by a WR star where $\text{He}^{++}/\text{He} = 0.4$. The principal difficulty with $S234$ is the inclusion of the mid-IR line $[\text{S IV}]\lambda 10.5\mu$, which is not readily observable with standard ground-based instrumentation. However, since the IP necessary to produce S^{+3} is virtually the same as that for O^{++} , it is possible to estimate the abundance of S^{+3} based on that for O^{++} . This was demonstrated earlier by Mathis (1982) and Dennefeld & Stasińska (1983). We present this approach here.

Figure 8 presents $\log(\text{S}/\text{H})$ vs. $S234$, on the same scale as that for $S23$ in Figure 7b. The line types and symbols are the same as before. We see that $S234$ is dramatically less sensitive to the ionization parameter, owing to the inclusion of the S IV indicator. Indeed, the models for $S234$ are even less sensitive to U than is $R23$ (Figure 7a), for $Z \lesssim Z_{\odot}$.

It would therefore be desirable to estimate the intensity of $[\text{S IV}]\lambda 10.5\mu$ from that of the O ionization indicator, $[\text{O III}]/[\text{O II}]$. Figure 9 shows $\log([\text{S IV}]\lambda 10.5\mu/[\text{S III}]\lambda\lambda 9069, 9532)$ vs. $\log([\text{O III}]\lambda\lambda 4959, 5007/[\text{O II}]\lambda 3727)$ for models with an E2 CoStar atmosphere, and line types as before. This atmosphere corresponds to an O3 – O4 stellar type, and we

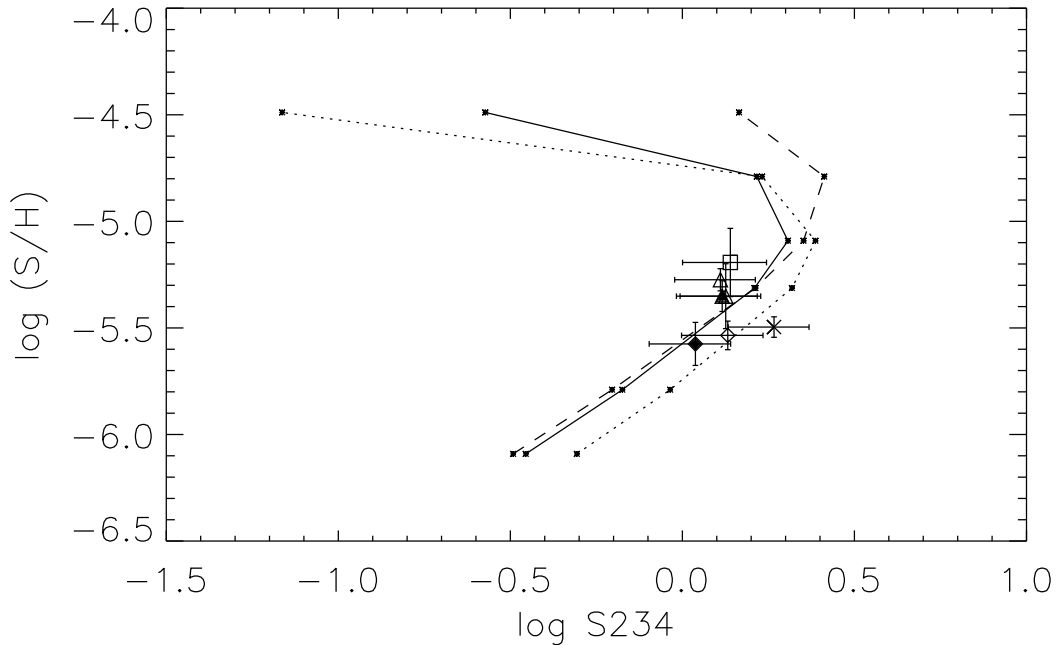


FIG. 8.— Photoionization models and data for $\log(S/H)$ vs. $S234$. As before, the tracks are computed for metallicities 0.05, 0.1, 0.3, 0.5, 1.0, and $2.0 Z_{\odot}$; and dashed, solid, and dotted linetypes correspond to $\log U = -2, -3,$ and $-4,$ respectively. Observed values for $S234$ are computed as described in the text, and are indicated by the symbols as in Figure 7.

prefer this model in examining the relation between S IV and other ions since it is more relevant in environments with harder ionizing fields. We see that for $Z \leq 0.5 Z_{\odot}$ (solid points), the relation between these ratios is essentially a simple power law. For these points, we fit:

$$\log \frac{[\text{S IV}]\lambda 10.5\mu}{[\text{S III}]\lambda\lambda 9069, 9532} = -0.984 + 1.276 \log \frac{[\text{O III}]\lambda\lambda 4959, 5007}{[\text{O II}]\lambda 3727} \quad (14)$$

which is shown by the dot-dashed line in Figure 9.

With observations of [S III], this relation allows an estimate of the [S IV] intensity, which can then be used to compute $S234$. We note that the adoption of the cooler C2 CoStar atmospheres, used in our other photoionization models, would result in a difference of less than 0.02 and 0.01 in the fitted intercept and slope, respectively. Furthermore, the correction for [S IV] will only be significant for moderate to high U and/or high Z . As a test of equation 14, we use mid-infrared and optical line observations of the Orion nebula by Lester, Dinerstein, & Rank (1979). For their measurements, equation 14 predicts a volume emissivity for [S IV] $\lambda 10.5\mu$ of $6.5 \pm 2.7 \times 10^{-21} \text{ erg cm}^{-6} \text{ s}^{-1}$, which agrees within measurement uncertainties with the observed value of $9.0 \pm 2.7 \times 10^{-21} \text{ erg cm}^{-6} \text{ s}^{-1}$. Considering the extremely narrow, $10''$ line of sight on the Orion nebula, and much higher density (10^4 cm^{-3}) than considered for our purposes, this agreement is highly encouraging.

It is thus relatively simple to convert from $S23$ into $S234$ and thereby almost eliminate the sensitivity to U . We used this method of estimating [S IV] to compute $S234$ for our spatially-integrated observations (Table 5), which are plot-

ted in Figure 8, using the same symbols as before. In the errors for $S234$, we include in quadrature an uncertainty of 25% for the uncertainty of [S IV] from equation 14. We again have excellent agreement with the models. It is clear that Z can be estimated with greater confidence based on $S234$ than $S23$ at these metallicities, because the large spread in the models for $S23$ (Figure 7b) has been vastly reduced for $S234$.

Similarly, we show in Figure 10 that spatial variations are also reduced from $S23$ to $S234$. Figures 10a and b show our spatially resolved observations of DEM L199 for $S23$ and $S234$. The solid line indicates the tailored model for this object, using the early WR model of Schmutz et al. (1992; see Paper I), central hole radius of $0.5 R_S$, and gas density $n = 100 \text{ cm}^{-3}$. While Figure 10a shows a large spatial variation of $\gtrsim 0.4$ dex for $S23$, we see in Figure 10b that the variation in $S234$ is reduced by about a factor of 2 in the logarithm. Figures 10e – f show the same behavior for DEM L323. The solid line again represents the corresponding tailored model, with an O3 – O4 stellar atmosphere (Costar E2), central hole radius of $0.4 R_S$, and gas density $n = 10 \text{ cm}^{-3}$. In Figure 10c – d, we show the spatially resolved data for DEM L199 superimposed on the model tracks for $S23$ and $S234$, respectively. The reduced scatter in $S234$ against the models again demonstrates the improved constraints in estimating $\log(S/H)$, compared to $S23$.

3.4. Calibrations

In Figure 11a and b we show the models for $\log(S/H)$ as a function of $S23$ and $S234$, overplotted with the Galactic and LMC data presented by Dennefeld & Stasińska

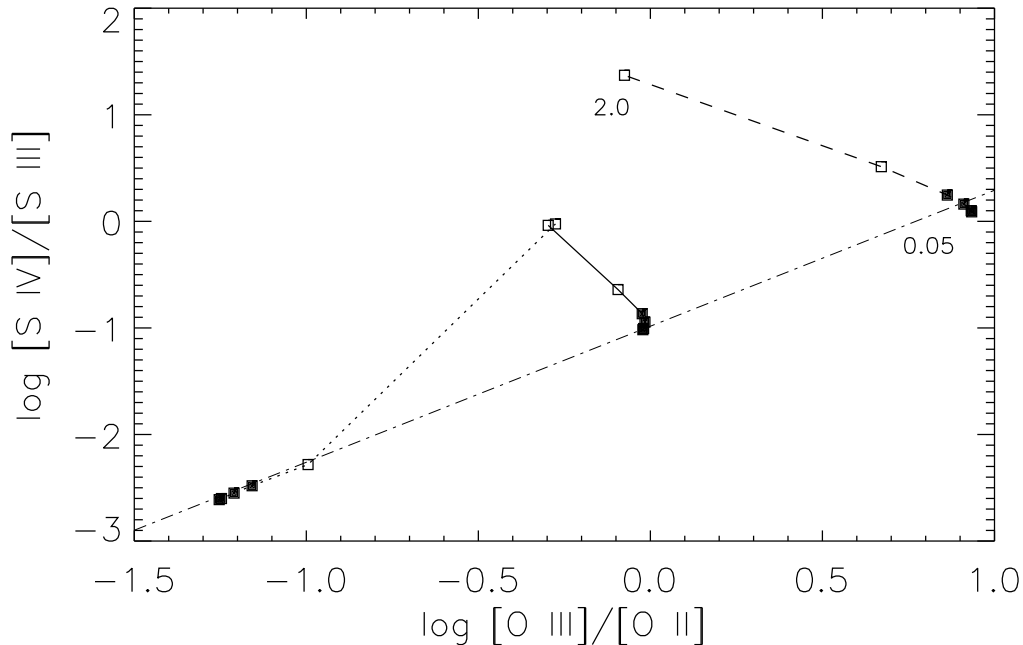


FIG. 9.— Models of $\log([\text{S IV}]\lambda 10.5\mu/[\text{S III}]\lambda\lambda 9069,9532)$ vs. $\log([\text{O III}]\lambda\lambda 4959,5007/[\text{O II}]\lambda 3727)$. These models employ the Costar E2 stellar atmosphere model. The line types are as before, and the metallicity extremes are indicated in solar units for the $U = -2$ track (models for 0.05 and $0.1 Z_{\odot}$ are virtually degenerate and indistinguishable). Equation 14 (dot-dashed line) is fitted from the solid points ($Z \leq 0.5 Z_{\odot}$).

(1983). Their S abundances are computed from measurements of $T[\text{O III}]$ and observations of $[\text{S III}]\lambda\lambda 9069,9532$. We compute $S234$ from this dataset with the aid of equation 14, as described above. Figure 11 shows that the data present a well-defined sequence in both $S23$ and $S234$. It is especially encouraging that the locus of the models is in excellent agreement with that of the data, in contrast with the situation for $R23$, as we saw above in Figure 7a. We replot the $R23$ models with the Dennefeld & Stasińska data in Figure 11c, again suggesting the same discrepancy seen earlier. It is apparent that for these data, the values of $R23$ are fairly insensitive to $\log(\text{O}/\text{H})$ as we saw before, owing to the location of the inflection and spread in U .

To estimate a theoretical calibration for $S23$, we take the mean of the three models at each metallicity, up to $0.5 Z_{\odot}$. A resulting power-law fit is shown by the lighter, straight, solid line in Figure 11a. For $S23$, we obtain:

$$\log(\text{S}/\text{H}) = -5.43 + 1.33 \log S23 \quad . \quad (15)$$

The light dash-dot and dashed lines in Figure 11a show the DPM and Christensen et al. (1997) calibrations, respectively. DPM calibrated a relation for $\log(\text{O}/\text{H})$ vs. $S23$, so we used the solar S/O ratio to convert their relation to a calibration of $\log(\text{S}/\text{H})$. It is apparent that all three calibrations are similar. The DPM relation shows the best correspondence to the data, as is expected since it is fitted to the largest dataset. It is especially encouraging that our theoretical relation is intermediate between the two empirical ones, confirming that the theoretical calibration is fully consistent with the available data. However, in using any of these $S23$ calibrations, it is important to bear

in mind that the models predict a double-valued relation around $\log S23 \gtrsim 0.0$.

We use the same procedure to fit a theoretical calibration for $S234$ and obtain:

$$\log(\text{S}/\text{H}) = -5.58 + 1.27 \log S234 \quad . \quad (16)$$

As in the case for $S23$, the data are in excellent agreement with this rough theoretical fit, shown by the light, solid line in Figure 11b.

We again emphasize that, although the data at $Z > 0.5 Z_{\odot}$ are consistent with the calibrations for both $S23$ and $S234$, they strongly diverge from the models in that regime, and that a power-law approximation is necessarily crude near these values. *We therefore consider the calibrations reliable only for $Z \lesssim 0.5 Z_{\odot}$* , and extreme caution should be exercised in extrapolating at higher metallicity. It is also essential to note that the double-valued nature of all of these abundance parameters still remains an issue.

In Figure 11d, we show the measured $\log(\text{O}/\text{H})$ vs. $\log S234$ for the Dennefeld & Stasińska sample, where $\log(\text{O}/\text{H})$ are again derived from direct measurements of $T[\text{O III}]$. We see that the scatter is much larger than for $\log(\text{S}/\text{H})$ vs. $\log S234$ (Figure 11b). Although Garnett (1989), among others, suggests that there is no systematic variation in S/O with O/H, Figure 11 shows that there is still significant variation in the S/O ratio among the different objects. Therefore, while $S234$ appears reasonably reliable for estimating the S abundance, it appears to be significantly less reliable for inferring the O abundance, and caution should be exercised accordingly.

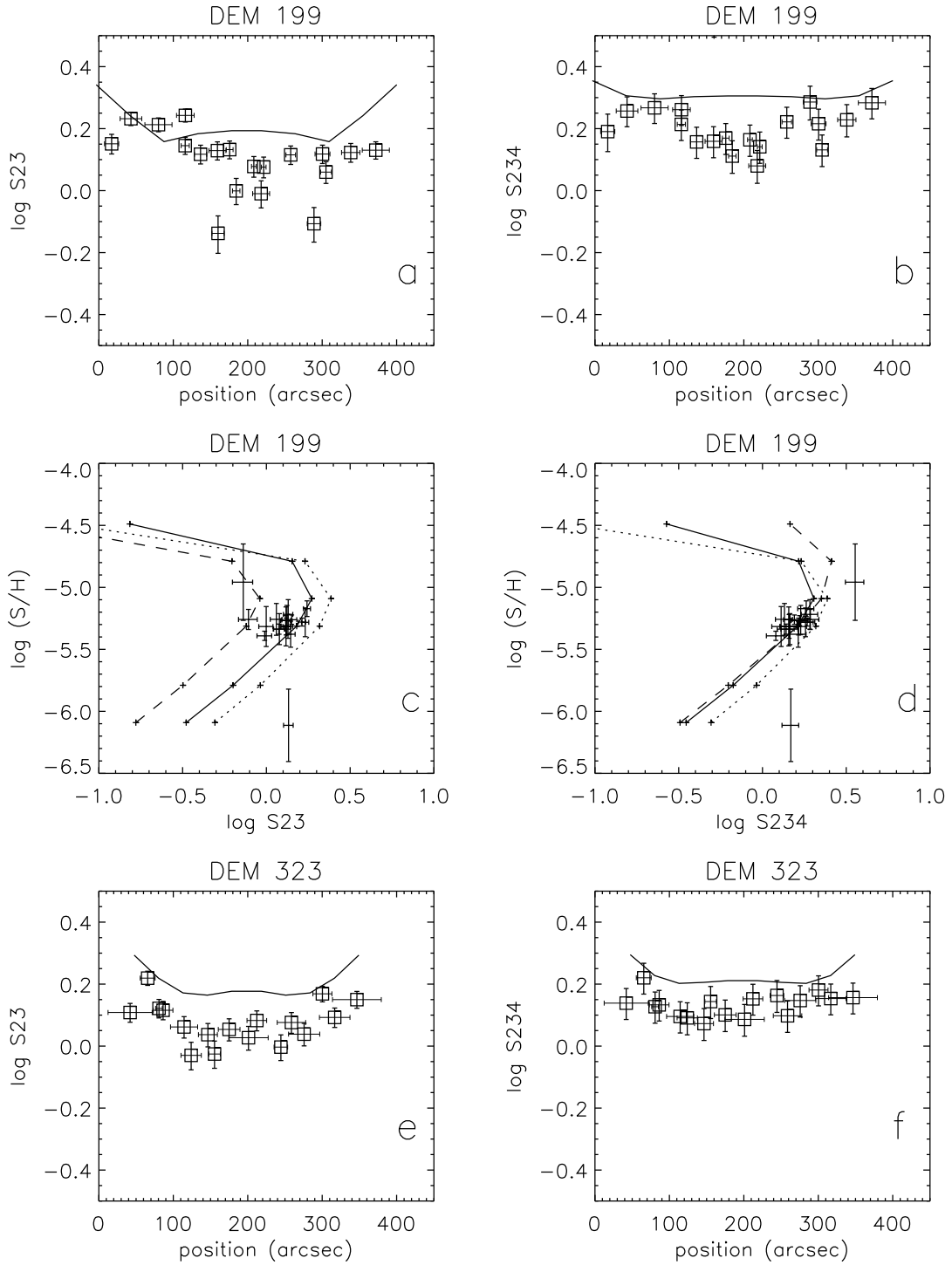


FIG. 10.— Spatial variation of S_{23} and S_{234} in DEM L199 (panels *a* and *b*) and DEM L323 (panels *e* and *f*). The light, horizontal bars indicate the spatial extent of the apertures for these data. Panels *c* and *d* show the same data for DEM L199 superimposed on the models, with linetypes as in Figure 7.

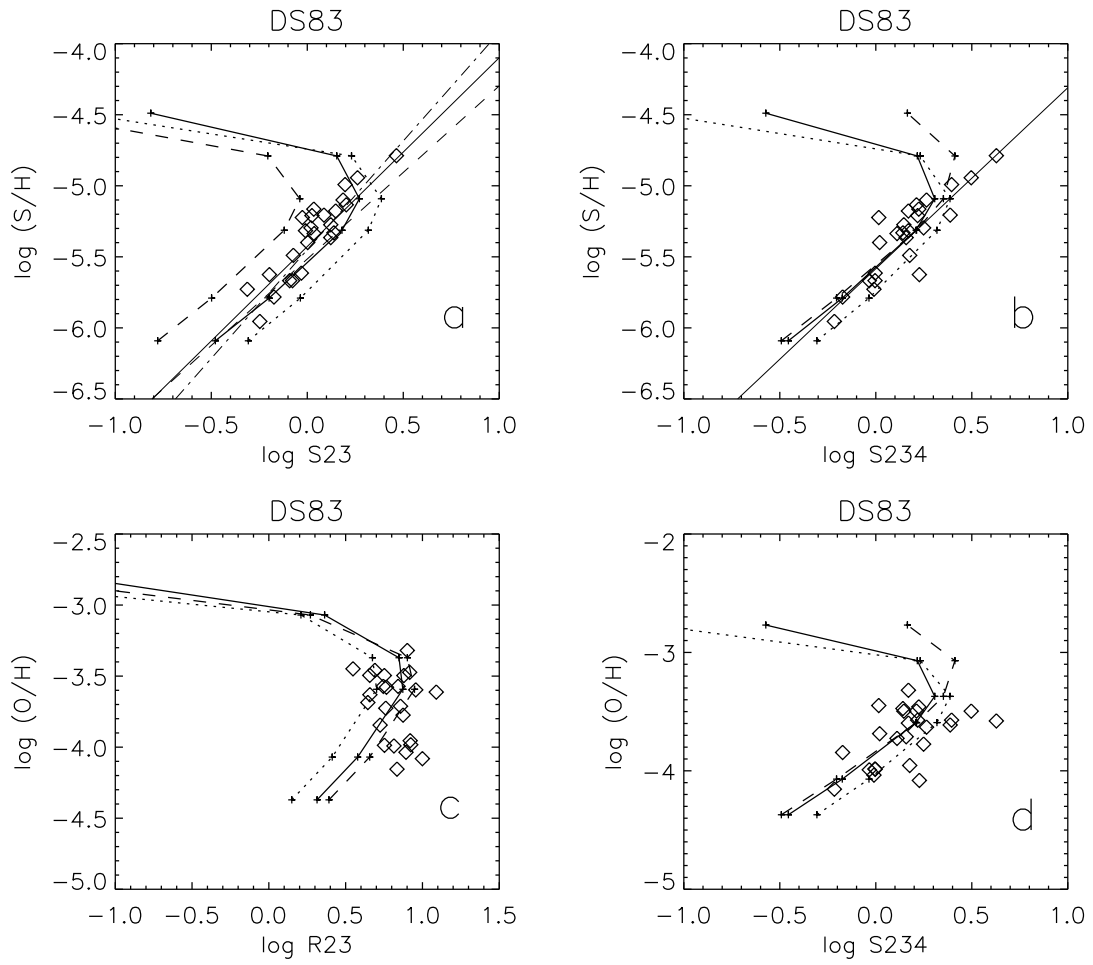


FIG. 11.— S abundance vs. diagnostics $S23$ (panel *a*) and $S234$ (panel *b*), and O abundance vs. $R23$ (panel *c*) and $S234$ (panel *d*). The models are the same as in Figures 7 and 8. Data points are from Dennefeld & Stasińska (1983), with $S234$ computed as described in the text. The lighter, solid lines show a fit to our models (see text), while the light, dot-dashed and dashed lines show the DPM and Christensen et al. (1997) empirical calibrations, respectively.

4. CONCLUSION

We have carried out a detailed investigation of elemental abundance derivations using four H II regions in the LMC. We use tailored photoionization models to examine standard abundance analyses based on measured values of T_e . Our data (Paper I) are derived from both spatially-resolved observations extracted from stationary long slit positions, and scanned, spatially-integrated slit observations. We also examine the bright-line abundance diagnostics for O and S, in light of the direct abundance determinations and photoionization models.

Our abundance determinations are based on measurements of $T[\text{O III}]$, which we take to represent $T(\text{O}^{++})$, and we assume a two-zone temperature structure for the nebulae, represented by $T(\text{O}^{++})$ and $T(\text{O}^+)$. We use standard ionic abundance relations to then determine the total elemental abundances for He, N, O, Ne, S, and Ar, with respect to H. Comparison with tailored MAPPINGS photoionization models highlights the importance of choosing a relation between $T(\text{O}^{++})$ and $T(\text{O}^+)$ that adequately represents the nebular temperature structure. Failure to do so can result in metallicity estimates that are discrepant by at least 0.2 dex from values indicated by tailored photoionization models.

Abundance measurements for the stationary slit positions show high spatial uniformity, with no evidence of variations or gradients to within 0.1 – 0.15 dex. Thus it is unlikely that there are systematic biases resulting from the strong ionization gradients seen in these objects. The adopted two-zone T_e structure therefore appears to be highly reliable for estimating ionic abundance estimates even through “pencil-beam” apertures that sample only a small nebular area, at least for our fairly isothermal H II regions.

No areas of local enrichment were detected in DEM L199, in spite of the presence of two WN3 stars and one WC4 star. The stellar products may be hidden in hot, coronal gas within the central superbubble, or the stars may not have produced enough enriched material to be readily detectable. The results show that self-enrichment by WR stars is likely to be a complex phenomenon, empirically. DEM L243 and DEM L301, both showing evidence of recent SNR activity, also do not show local enrichments, although with poorer constraints.

Abundance measurements from the scanned, spatially integrated apertures are consistent with those obtained from the spatially resolved observations. Our results are ~ 0.2 dex lower than average LMC H II region measurements (Dufour 1984; Garnett 1999), probably resulting in part from different descriptions for the T_e structure. The spatially-integrated measurements are also consistent with there being no variation between the four H II regions, although, interestingly, they are also consistent with the marginal abundance gradient suggested by Pagel et al. (1978). While the presence of the SNR in DEM L243 did not affect the resulting abundances from the spatially integrated observation, the derived abundances for DEM L301 are on the low end of the distribution, hinting at spurious effects caused by the shock activity in that superbubble.

We computed the $R23$ O abundance parameters (Pagel et al. 1979) for the spatially integrated data, and compared

these with model tracks constructed with MAPPINGS. The models assume the Costar C2 (Schaerer & de Koter 1997) stellar atmosphere corresponding to an O6 – O7 spectral type, and an inner nebular radius of $0.4 R_S$. As has historically been the case, the models do not agree well with the locus of observations in the literature, although our LMC data do agree well, coincidentally, with both.

Similarly, we examined the $S23$ abundance parameter for S (e.g., Christensen et al. 1997; Díaz & Pérez-Montero 2000). Our models reveal that, contrary to previous suggestions, $S23$ is *more* sensitive to the ionization parameter than is $R23$. S IV is produced by the same radiation that ionizes O III, and is a significant ion of S in many H II regions, but it is not sampled by $S23$. Its omission therefore causes $S23$ to be much more sensitive to U than $R23$. The spatially resolved observations confirm this by showing, in agreement with model predictions, lower values of $S23$ in the central nebular regions where S IV is important. As shown in Paper I, this spatial variation is not predicted or observed in $R23$.

Our models also suggest that the maximum in $S23$ occurs at only ~ 0.2 dex higher in Z than in $R23$. Nevertheless, this appears to significantly alleviate the effect of the double-valued structure of $\log(\text{S}/\text{H})$ vs $S23$ when inferring abundances, as shown by Díaz & Pérez-Montero (2000). It is highly encouraging that the data, both from our sample and from the literature, are in excellent agreement with the models, in contrast to the behavior of $R23$. We offer a theoretical calibration of $S23$ (equation 15) which appears to be fully compatible with the data in the literature thus far. However, we caution that the locus of the available data may well be deceptive in suggesting that a power-law relation can be used at $Z \gtrsim 0.5 Z_\odot$.

To overcome the limitations of $S23$ in U -sensitivity and spatial variation, we introduce a similar S abundance parameter, $S234$. This is the same as $S23$ with the added emission of $[\text{S IV}]\lambda 10.5\mu$. Although this mid-IR line is not readily observable with most conventional ground-based spectrographs, it is straightforward to estimate its intensity from the simple correspondence between $[\text{S IV}]/[\text{S III}]$ and $[\text{O III}]/[\text{O II}]$ (equation 14). Our models show that $S234$ is less dependent on U than is even $R23$. $S234$ for our objects and for the larger sample of Dennefeld & Stasińska (1983) are in excellent agreement with the models. Likewise, the spatial variations for both models and observations are dramatically reduced for $S234$ in contrast to $S23$. We provide a theoretical calibration for $\log(\text{S}/\text{H})$ vs $S234$ at $Z \lesssim 0.5 Z_\odot$ (equation 16).

Finally, we reiterate some caveats for the use of $R23$, $S23$, and $S234$. We find that the presence of shock excitation increases the value of these parameters; for our objects, the effect is about 0.1 dex in magnitude. Secondly, significant variations in the S/O ratio dictate caution in inferring O abundances using $S234$ and $S23$ (Figure 11). It is also important to bear in mind the double-valued structure for all three of these parameters. Lastly, we emphasize the deviation between the data and models above $0.5 Z_\odot$, and we therefore consider the calibrations presented thus far for $S23$ and $S234$ to be reliable only for $Z \lesssim 0.5 Z_\odot$. Further empirical investigation is needed to understand the behavior of these parameters at higher metallicity. Bearing in mind these caveats, the excellent correspondence between the modeled $S234$, $S23$, and the

available data, together with the more highly monotonic behavior of these parameters, promises greater effectiveness as metallicity indicators than $R23$. With improving access to the $[\text{S IV}]\lambda 10.5\mu$ line, it should be possible to confirm the behavior of $S234$ directly.

It is a pleasure to acknowledge discussions with Mike Dopita, Annette Ferguson, Don Garnett, Dick Shaw, Evan Skillman, Elena Terlevich, and Bob Williams. We are also grateful to Mike Dopita for access to the MAPPINGS II photoionization code and to Angeles Díaz for access to her work in advance of publication. Finally, we are pleased to acknowledge the referee, Bernard Pagel.

TABLE 1
H II REGION SAMPLE

DEM	Henize	LH	Sp. Type	$\log(L_{H\alpha}/\text{erg s}^{-1})$ ^a	Inner radius	Shocks	Sp. Type Reference
DEM L199	N144	LH 58	WN3	38.6	$0.5 R_S$ ^b	no	Breysacher (1981)
DEM L243	N63 A	LH 83	O7	37.7	$0.1 R_S$	yes	Oey (1996a)
DEM L301	N70	LH 114	O3	37.7 ^c	$0.95 R_S$	yes	Oey (1996a)
DEM L323	N180 B	LH 117	O3-4	38.4 ^d	$0.4 R_S$	no	Massey et al. (1989)

^aFrom Oey & Kennicutt (1997), unless otherwise indicated.

^bDEM L199 has complex morphology (see Paper I).

^cDEM L301 is significantly density-bounded (Paper I).

^dKennicutt (1997), private communication.

TABLE 2
LOGARITHMIC ABUNDANCES OF SPATIALLY RESOLVED OBSERVATIONS^a

Observation	[He/H] ^b	err	[N/H]	err	[O/H]	err	[Ne/H] ^c	err	[S/H]	err	[Ar/H]	err
D199.205-ap10	-1.059	0.026	-4.892	0.126	-3.647	0.216	-4.390	0.256	-5.282	0.116	-5.993	0.133
D199.205-ap11	-1.091	0.021	-4.899	0.044	-3.633	0.065	-4.374	0.076	-5.261	0.038	-5.896	0.046
D199.205-ap13	-1.039	0.015	-4.890	0.040	-3.621	0.056	-4.368	0.064	-5.280	0.032	-5.889	0.040
D199.205-ap14	-1.066	0.020	-4.977	0.076	-3.571	0.130	-4.409	0.158	-5.172	0.063	-5.583	0.080
D199.205-ap15	-1.057	0.026	-4.927	0.118	-3.681	0.204	-4.483	0.241	-5.378	0.105	-5.886	0.125
D199.205-ap16	-1.016	0.027	-4.946	0.175	-3.421	0.313	-4.080	0.372	-5.315	0.157	-5.790	0.186
D199.205-ap17	-1.081	0.029	-4.947	0.104	-3.689	0.182	-4.537	0.225	-5.315	0.096	-5.924	0.113
D199.205-ap18	-1.001	0.069	-4.545	0.327	-3.018	0.587	-3.635	0.706	-4.958	0.308	-5.577	0.358
D199.205N120-ap10	-1.065	0.029	-4.928	0.178	-3.669	0.302	-4.316	0.359	-5.316	0.161	-6.010	0.186
D199.205N120-ap11	-1.065	0.027	-4.932	0.137	-3.627	0.237	-4.337	0.283	-5.337	0.125	-5.960	0.147
D199.205N120-ap12	-1.083	0.015	-4.999	0.043	-3.771	0.063	-4.553	0.074	-5.391	0.037	-6.104	0.047
D199.205N120-ap13	-1.088	0.018	-4.950	0.046	-3.695	0.072	-4.423	0.085	-5.337	0.041	-5.992	0.049
D199.205N120-ap14	-1.011	0.015	-4.898	0.047	-3.552	0.073	-4.317	0.085	-5.268	0.040	-5.814	0.049
D199.205N120-ap15	-1.033	0.019	-4.942	0.077	-3.573	0.130	-4.344	0.154	-5.316	0.068	-5.867	0.081
D199.205N120-ap16	-1.031	0.019	-4.869	0.089	-3.569	0.154	-4.347	0.184	-5.259	0.081	-5.815	0.097
D199.205N120-ap17	-1.033	0.027	-5.205	0.161	-3.522	0.296	-4.271	0.334	-5.264	0.118	-5.674	0.148
D199.205N120-ap18	-1.046	0.027	-4.905	0.141	-3.382	0.252	-4.071	0.301	-5.258	0.128	-5.755	0.151
D199.205N120-ap19	-1.014	0.024	-4.909	0.131	-3.578	0.230	-4.304	0.275	-5.218	0.119	-5.763	0.143
D243.2S-ap6	-1.068	0.026	-5.412	0.110	-4.177	0.175	-5.306	0.242	-5.710	0.095	-6.360	0.115
D243.2S-ap9	-1.176	0.025	-5.279	0.151	-4.094	0.257	-5.064	0.303	-5.683	0.136	-6.393	0.158
D243.2S-ap14	-1.313	0.031	-5.252	0.108	-4.055	0.173	-4.940	0.206	-5.643	0.098	-6.570	0.119
D243.5S-ap3	-1.559	0.069	-5.408	0.350	-4.337	0.563	-5.442	0.775	-5.801	0.317	-7.030	0.338
D243.5S-ap6	-1.296	0.023	-5.079	0.177	-3.703	0.305	-4.675	0.363	-5.414	0.159	-6.200	0.182
D243.5S-ap5	-1.101	0.019	-5.074	0.064	-3.587	0.107	-4.457	0.130	-5.375	0.056	-5.931	0.066
D243.5S-ap7	-1.156	0.034	-4.843	0.290	-3.315	0.507	-4.215	0.607	-5.246	0.262	-5.885	0.297
D243.5S-ap8	-1.161	0.039	-5.085	0.263	-3.634	0.452	-4.654	0.556	-5.406	0.235	-6.073	0.276
D243.30S-ap9	-1.293	0.125	-5.412	0.319	-4.397	0.520	-5.678	0.720	-5.803	0.298	-6.617	0.323
D243.30S-ap10	-1.146	0.047	-5.219	0.189	-3.944	0.317	-4.951	0.400	-5.526	0.169	-6.242	0.198
D243.30S-ap11	-1.164	0.036	-4.763	0.298	-3.147	0.522	-4.079	0.641	-5.191	0.270	-5.769	0.312
D243.30S-ap14	-1.257	0.077	-5.413	0.240	-4.332	0.397	-5.398	0.524	-5.786	0.222	-6.594	0.254
D243.30S-ap15	-1.108	0.098	-4.587	0.320	-2.909	0.549	-3.563	0.675	-4.980	0.292	-5.608	0.340
D243fix.2S-ap6	-1.083	0.025	-5.145	0.065	-3.745	0.100	-4.796	0.150	-5.476	0.054	-6.072	0.068
D243fix.2S-ap9	-1.185	0.024	-5.083	0.055	-3.778	0.089	-4.687	0.116	-5.508	0.048	-6.180	0.058
D243fix.2S-ap14	-1.332	0.030	-4.991	0.056	-3.633	0.091	-4.441	0.114	-5.405	0.051	-6.289	0.071
D243fix.5S-ap3	-1.575	0.079	-5.085	0.057	-3.813	0.091	-4.824	0.411	-5.513	0.048	-6.693	0.095
D243fix.5S-ap6	-1.295	0.022	-5.095	0.054	-3.731	0.089	-4.708	0.109	-5.428	0.049	-6.216	0.058
D243fix.5S-ap5	-1.096	0.019	-5.167	0.055	-3.755	0.087	-4.657	0.109	-5.459	0.049	-6.031	0.058
D243fix.5S-ap7	-1.143	0.031	-5.096	0.056	-3.757	0.090	-4.737	0.135	-5.473	0.053	-6.144	0.066
D243fix.5S-ap8	-1.158	0.037	-5.130	0.059	-3.713	0.089	-4.747	0.160	-5.447	0.052	-6.120	0.075
D243fix.30S-ap9	-1.305	0.132	-5.010	0.058	-3.748	0.092	-4.919	0.432	-5.446	0.055	-6.196	0.090
D243fix.30S-ap10	-1.150	0.047	-5.078	0.056	-3.715	0.089	-4.678	0.176	-5.400	0.050	-6.089	0.063
D243fix.30S-ap11	-1.151	0.033	-5.086	0.054	-3.722	0.087	-4.760	0.192	-5.484	0.050	-6.107	0.060
D243fix.30S-ap14	-1.283	0.076	-5.089	0.059	-3.810	0.092	-4.783	0.278	-5.493	0.059	-6.247	0.075
D243fix.30S-ap15	-1.084	0.097	-5.063	0.065	-3.759	0.093	-4.573	0.236	-5.421	0.059	-6.105	0.092
D301.SW6-ap7	-1.061	0.019	-5.193	0.059	-3.984	0.092	-4.695	0.111	-5.487	0.052	-6.323	0.063
D301.SW6-ap8	-1.031	0.020	-5.116	0.062	-3.874	0.097	-4.672	0.118	-5.445	0.055	-6.205	0.067
D301.SW6-ap9	-1.065	0.020	-4.975	0.199	-3.667	0.336	-4.377	0.397	-5.279	0.178	-6.052	0.199
D301.SW6-ap10	-0.920	0.025	-5.071	0.064	-3.820	0.101	-4.475	0.120	-5.411	0.057	-6.144	0.070
D301.SW6-ap11	-1.036	0.020	-5.163	0.062	-3.912	0.098	-4.743	0.125	-5.439	0.055	-6.228	0.067
D301.SW1-ap6	-1.135	0.032	-5.008	0.309	-3.710	0.514	-4.190	0.607	-5.362	0.277	-6.254	0.305
D301.SW1-ap5	-1.088	0.018	-4.980	0.195	-3.518	0.334	-4.437	0.395	-5.297	0.169	-5.984	0.193
D323.C2-ap7	-1.194	0.022	-5.127	0.105	-3.597	0.180	-4.519	0.213	-5.327	0.090	-5.958	0.109
D323.C2-ap8	-1.089	0.017	-5.168	0.070	-3.710	0.114	-4.625	0.135	-5.421	0.060	-6.040	0.074
D323.C2-ap9	-1.072	0.016	-5.084	0.048	-3.594	0.078	-4.437	0.091	-5.349	0.042	-5.942	0.051
D323.C2-ap10	-1.190	0.021	-5.113	0.042	-3.627	0.060	-4.483	0.069	-5.323	0.035	-5.908	0.042
D323.C2-ap11	-1.049	0.016	-5.149	0.058	-3.639	0.089	-4.488	0.102	-5.316	0.046	-5.843	0.056
D323.C2-ap12	-1.057	0.016	-5.127	0.053	-3.631	0.082	-4.511	0.096	-5.294	0.043	-5.883	0.051
D323.C2-ap13	-1.066	0.027	-5.268	0.083	-3.852	0.130	-4.782	0.159	-5.419	0.072	-6.074	0.088
D323.C1-ap13	-1.080	0.051	-4.995	0.302	-3.461	0.526	-4.341	0.639	-5.265	0.262	-5.885	0.313
D323.C1-ap6	-1.169	0.019	-4.919	0.127	-3.361	0.219	-4.255	0.259	-5.207	0.108	-5.912	0.127
D323.C1-ap7	-1.175	0.022	-5.238	0.053	-3.660	0.088	-4.575	0.104	-5.345	0.046	-5.891	0.054
D323.C1-ap8	-1.050	0.016	-5.178	0.052	-3.635	0.082	-4.513	0.095	-5.306	0.043	-5.835	0.051
D323.C1-ap9	-1.077	0.016	-5.165	0.033	-3.602	0.044	-4.454	0.050	-5.361	0.028	-5.920	0.032
D323.C1-ap10	-1.085	0.017	-5.112	0.067	-3.618	0.112	-4.525	0.132	-5.359	0.058	-5.993	0.070
D323.C1-ap11	-1.059	0.016	-5.133	0.040	-3.678	0.063	-4.763	0.080	-5.316	0.036	-5.995	0.042
D323.C1-ap12	-1.113	0.029	-5.149	0.253	-3.713	0.425	-4.530	0.513	-5.391	0.217	-6.159	0.252

^aD243fix observations have values computed for $T(O^{++})$ fixed at 9700 K.

^b[He/H] are lower limits for DEM L243.

^c[Ne/H] is subject to systematic uncertainties (see text).

TABLE 3
MEAN LOGARITHMIC ABUNDANCES FROM SPATIALLY RESOLVED OBSERVATIONS

Object	$T[\text{O III}](\text{K})$	σ	[He/H]	σ	[N/H]	σ	[O/H]	σ	[Ne/H] ^a	σ	[S/H]	σ	[Ar/H]	σ
DEM L199	9620	140	-1.05	0.005	-4.93	0.017	-3.64	0.026	-4.40	0.030	-5.30	0.014	-5.90	0.018
DEM L243	9620	360	-1.18 ^b	0.009	-5.17	0.040	-3.83	0.068	-4.75	0.084	-5.50	0.036	-6.18	0.043
DEM L243 ^c	9700	...	-1.18 ^b	0.009	-5.09	0.016	-3.74	0.025	-4.67	0.042	-5.46	0.014	-6.17	0.019
DEM L301	11900	420	-1.05	0.008	-5.13	0.030	-3.89	0.047	-4.63	0.058	-5.44	0.027	-6.22	0.032
DEM L323	9480	110	-1.09	0.005	-5.15	0.015	-3.63	0.022	-4.52	0.026	-5.33	0.012	-5.93	0.015

^a[Ne/H] is subject to systematic uncertainties (see text).

^b[He/H] is a lower limit in this object.

^c $T(\text{O}^{++})$ fixed at 9700 K for all apertures.

TABLE 4
LOGARITHMIC ABUNDANCES FROM SPATIALLY INTEGRATED OBSERVATIONS

Observation	$T[\text{O III}](\text{K})$	err	[He/H]	err	[N/H]	err	[O/H]	err	[Ne/H] ^a	err	[S/H]	err	[Ar/H]	err
D199.496W240	8100	1100	-1.13	0.03	-4.77	0.17	-3.31	0.31	-3.97	0.37	-5.19	0.16	-5.73	0.18
D243.2(total)	11900	1000	-1.18	0.02	-5.24	0.08	-4.01	0.12	-4.90	0.14	-5.54	0.07	-6.36	0.08
D243.2(no SNR)	11400	1400	-1.17	0.03	-5.26	0.12	-3.97	0.19	-4.90	0.23	-5.58	0.10	-6.26	0.12
D301.SW6	13000	900	-1.04	0.02	-5.19	0.06	-3.94	0.09	-4.66	0.10	-5.50	0.05	-6.27	0.06
D323.140(total)	9600	700	-1.09	0.02	-5.10	0.08	-3.64	0.14	-4.54	0.17	-5.35	0.07	-5.97	0.09
D323.140N30N	9700	1400	-1.11	0.03	-5.13	0.18	-3.66	0.30	-4.57	0.36	-5.35	0.15	-6.04	0.18
D323.140N30S	8800	400	-1.21	0.02	-5.02	0.06	-3.48	0.10	-4.30	0.12	-5.27	0.05	-5.85	0.06
Dufour (1984) ^b			-1.07	0.02	-5.03	0.10	-3.57	0.08	-4.36	0.10	-5.15	0.11	-5.80	0.06

^a[Ne/H] is subject to systematic uncertainties (see text).

^bMean LMC H II region abundances as compiled by Dufour (1984).

TABLE 5
ABUNDANCE PARAMETERS FOR SPATIALLY INTEGRATED OBSERVATIONS

Observation	$R23^a$	err	$S23^a$	err	$S234^b$	err
D199.496W240	6.9	0.4	1.11	0.08	1.38	0.38
D243.2 (total)	4.7	0.5	1.31	0.08	1.35	0.36
D243.2 (no SNR)	4.7	0.5	1.04	0.07	1.09	0.29
D301.SW6	7.1	0.9	1.83	0.11	1.85	0.49
D323.140	6.1	0.5	1.19	0.08	1.31	0.34
D323.140N30N	5.8	0.6	1.27	0.09	1.34	0.35
D323.140N30S	6.2	0.5	1.15	0.08	1.29	0.34

^aFrom Paper I.

^bComputed by estimating [S IV] with equation 14.

REFERENCES

- Anders, E. & Grevesse, N., 1989, *Geochim. Cosmochim. Acta*, 53, 197
- Baldwin, J. A., Ferland, G. J., Martin, P. G., Corbin, M. R., Cota, S. A., Peterson, B. M., & Slettebak, A., 1991, *ApJ*, 374, 580.
- Breysacher, J., 1981, *AAS*, 43, 203
- Benjamin, R. A., Skillman, E. D., & Smits, D. P. 1999, *ApJ*, 514, 307
- Campbell, A., Terlevich, R., & Melnick, J., 1986, *MNRAS*, 223, 811
- Christensen, T., Petersen, L. & Gammelgaard, P., 1997, *AA*, 322, 41
- Chu, Y-H. & Mac Low, M-M., 1990, *ApJ*, 365, 510
- Davies, R. D., Elliott, K. H., & Meaburn, J., 1976, *Mem. RAS*, 81, 89
- Dennefeld, M. & Stasińska, G., 1983, *AA*, 118, 234
- Díaz, A. I. & Pérez-Montero, E., 2000, *MNRAS*, 312, 130
- Díaz, A. I., Terlevich, E., Pagel, B. E. J., Vilchez, J. M., & Edmunds, M. G. 1987, *MNRAS*, 226, 19
- Dopita, M. A. & Evans, I. N., 1986, *ApJ*, 307, 431
- Dufour, R. J., 1984, in *Structure and Evolution of the Magellanic Clouds*, IAU Symp 108, S. van den Bergh & K. S. de Boer, eds., (Dordrecht: Reidel), 353
- Garnett, D. R., 1989, *ApJ*, 345, 282
- Garnett, D. R., 1990, *ApJ*, 363, 142
- Garnett, D. R., 1992, *AJ*, 103, 1330
- Garnett, D. R., Shields, G. A., Skillman, E. D., Sagan, S. P., & Dufour, R. J., 1997, *ApJ*, 489, 63
- Garnett, D. R., 1999, in *New Views of the Magellanic Clouds*, IAU Symp. 190, Y.-H. Chu, N. Suntzeff, J. Hesser, & D. Bohlender, eds., (San Francisco: ASP), 266
- González-Delgado, R. M. et al. 1994, *ApJ*, 437, 239
- Gruenwald, R. B., & Viegas, S. M. 1992, *ApJS*, 78, 153
- Hamann, W-R. & Koesterke, L., 1998, *AA*, 333, 251; HK98
- Hummer, D. G. & Mihalas, D. M., 1970, *MNRAS*, 147, 339
- Henize, K. G., 1956, *ApJS*, 2, 315
- Kennicutt, R. C., Bresolin, F., French, H., & Martin, P., 2000, *ApJ*, in press; astro-ph/0002180
- Kobulnicky, H. A., Kennicutt, R. C., & Pizagno, J. L., 1999, *ApJ*, 514, 544
- Kobulnicky, H. A., & Skillman, E. D. 1996, *ApJ*, 471, 211
- Kobulnicky, H. A., Skillman, E. D., Roy, J.-R., Walsh, J. R., & Rosa, M. R., 1997, *ApJ*, 477, 679
- Kurucz, R. L., 1991, in *Stellar Atmospheres: Beyond Classical Models*, L. Crivellari, I. Hubeny, & D. G. Hummer, eds., NATO ASI Series C, Vol. 341, 441
- Lester, D. G., Dinerstein, H. L., & Rank, D. M., 1979, *ApJ*, 232, 139
- Lucke, P. B. & Hodge, P. W., 1970, *AJ*, 75, 171
- Masegosa, J., Moles, M., & del Olmo, A. 1991, *A&A*, 249, 505
- Massey, P., Garmany, C. D., Silkey, M., & DeGioia-Eastwood, K., 1989, *AJ*, 97, 107
- Mathis, J. S., 1982, *ApJ*, 261, 195
- Mathis, J. S., 1985, *ApJ*, 291, 247
- Mathis, J. S., 1995, *Rev.Mex.Astron.Astrof., Ser.Conf.*, 3, 207
- McGaugh, S. S., 1991, *ApJ*, 380, 140
- Moffat, A. F. J., Niemela, V. S., & Marraco, H. G., 1990, *ApJ*, 348, 232
- Oey, M. S., 1996a, *ApJ*, 465, 231
- Oey, M. S., 1996b, *ApJ*, 467, 666
- Oey, M. S. & Kennicutt, R. C., 1997, *MNRAS*, 291, 827
- Oey, M. S., Dopita, M. A., Shields, J. C., & Smith, R. C., 2000, *ApJS*, in press (Paper I); astro-ph/9912363
- Olszewski, E. W., Schommer, R. A., Suntzeff, N. B., & Harris, H. C., 1991, *AJ*, 101, 515
- Pagel, B. E. J., Edmunds, M. G., Fosbury, R. A. E., & Webster, B. L., 1978, *MNRAS*, 184, 569
- Pagel, B. E. J., Edmunds, M. G., Blackwell, D. E., Chun, M. S., & Smith, G., 1979, *MNRAS*, 189, 95
- Pagel, B. E. J., Simonson, E. A., Terlevich, R. J., & Edmunds, M. G., 1992, *MNRAS*, 255, 325
- Peimbert, M., 1967, *ApJ*, 150, 825
- Peimbert, M., 1993, *Rev.Mex.Astron.Astrof.*, 27, 9
- Peimbert, M., Sarmiento, A., & Fierro, J., 1991, *PASP*, 103, 815
- Peimbert, M. & Torres-Peimbert, S., 1977, *MNRAS*, 179, 217
- Russell, S. C. & Dopita, M. A., 1990, *ApJS*, 74, 93
- Schaerer, D. & de Koter, A., 1997, *AA*, 322, 598
- Schmutz, W., Leitherer, C., & Gruenwald, R., 1992, *PASP*, 104, 1164; SLG92
- Shaw, R. A., & Dufour, R. J. 1995, *PASP*, 107, 896
- Shields, J. C., & Kennicutt, R. C. 1995, *ApJ*, 454, 807
- Simpson, J. P., Colgan, S. W. J., Rubin, R. H., Erickson, E. F., & Haas, M. R., 1995, *ApJ*, 444, 721
- Skillman, E. D., 1989, *ApJ*, 347, 883
- Skillman, E. D. & Kennicutt, R. C., 1993, *ApJ*, 411, 655
- Stasińska, G., 1978, *AA*, 66, 257
- Stasińska, G., 1980, *AA*, 85, 359
- Stevenson, C. C., 1994, *MNRAS*, 267, 904
- Sutherland, R. S. & Dopita, M. A., 1993, *ApJS*, 88, 253
- Vilchez, J. M. & Esteban, C., 1996, *MNRAS*, 280, 720
- Vilchez, J. M. & Pagel, B. E. J., 1988, *MNRAS*, 231, 257
- Walsh, J. R. & Roy, J.-R., 1989, *MNRAS*, 239, 297
- Walter, D. K., Dufour, R. J., & Hester, J. J., 1992, *ApJ*, 397, 196